

Demonstrating Quantum Speed-Up with a Two-Transmon Quantum Processor.

Andreas Dewes

May 7, 2012

Contents

1	Introduction & Summary	11
1.1	Quantum Computing & Circuit Quantum Electrodynamics	11
1.2	Realizing a Two-Qubit Quantum Processor	13
1.3	Demonstrating Simultaneous Single-Shot Readout	14
1.4	Generating and Characterizing Entanglement	15
1.5	Realizing a Universal Two-Qubit Quantum Gate	18
1.6	Running a Quantum Search Algorithm	19
1.7	Demonstrating Quantum Speed-Up	21
1.8	Designing a Scalable Quantum Computing Architecture	21
2	Theoretical Foundations	23
2.1	Quantum Mechanics & Quantum Computing	23
2.2	Transmon Qubits	23
2.3	Circuit Quantum Electrodynamics	24
2.3.1	Dispersive Limit & Qubit Readout	24
2.4	The Josephson Bifurcation Amplifier	25
3	Realizing a Two-Qubit Processor	27
3.1	Introduction & Motivation	27
3.2	Qubit Design	28
3.3	Readout Design	28
3.4	Processor Fabrication	28
4	Measurement Setup	29
4.1	Sample Holder & PCB	29
4.2	Cryogenic Wiring	30
4.3	Signal Generation & Acquisition	31
4.3.1	Microwave Sideband Mixing	31
4.3.2	Fast Magnetic Flux Pulses	32
4.3.3	Pulse Synchronization	33

5 Measurement Techniques	35
5.1 Qubit Readout	35
5.2 Qubit Manipulation	35
5.3 Decoherence Time Measurement	35
6 Characterizing the Two-Qubit Processor	37
6.1 Qubit & Readout Characterization	37
6.1.1 Qubit Parameters	38
Readout Parameters	38
Qubit Readout, Driving, Relaxation and Dephasing Time	38
6.2 Single-Qubit Operations	40
6.3 Two Qubit Operations	41
6.3.1 Creation of Entanglement	41
6.3.2 Violation of the Bell Inequality	41
6.3.3 Quantum State Tomography of Two-Qubit States	41
Maximum Likelihood Estimation of Quantum States	42
6.4 Realizing a Two-Qubit Gate	44
6.4.1 Principle	44
6.4.2 Experimental Implementation	44
6.4.3 Quantum Process Tomography of the Gate	44
Introduction & Principle	44
Implementation	44
The Kraus Representation of the Quantum Process	48
6.4.4 Gate Fidelity	49
6.4.5 Gate Error Analysis	49
7 Running the Grover Search Algorithm	53
7.1 Introduction & Motivation	53
7.1.1 Ancilla-based Implementation of the Algorithm	56
7.2 Experimental Implementation	57
7.2.1 Pulse Sequence	58
7.3 Algorithm Fidelity	58
7.4 Comparision to a Classical Algorithm	60
7.5 Error Analysis	61
7.5.1 Gate Errors & Decoherence	61
Decoherence	61
Fidelity of the Oracle and diffusion operators	63
7.5.2 Readout Errors	65
7.6 Conclusions	66

<i>CONTENTS</i>	5
-----------------	---

8 Designing a Scalable Architecture for Quantum Bits	67
8.1 Definition & Requirements	68
8.2 Qubit Design	68
8.2.1 Qubit Parameters	68
8.2.2 Qubit-Qubit Coupling	68
8.3 Readout Design	68
8.3.1 Readout Parameters	68
8.3.2 Qubit-Readout Coupling	68
8.4 Single-Qubit Manipulation	68
8.4.1 Error Analysis	68
8.5 Multi-Qubit Manipulation	68
8.5.1 Error Analysis	68
8.6 Implementing a Universal Set of Quantum Gates	68
8.7 Realizing A Four-Qubit Architecture	68
8.8 Scaling Up	68
9 Conclusions & Outlook	69
9.1 Future Directions in Superconducting QC	69
9.1.1 3D Circuit Quantum Electrodynamics	69
9.1.2 Hybrid Quantum Systems	69
9.1.3 Quantum Error Correction & Feedback	69
A Modeling of Multi-Qubit Systems	71
A.1 Analytical Approach	71
A.1.1 Multi-Qubit Hamiltonian	71
A.1.2 Energies and Eigenstates	71
A.2 Master Equation Approach	71
A.2.1 Direct Integration	71
A.2.2 Monte Carlo Simulation	71
A.2.3 Speeding Up Simulations	71
B Data Acquisition & Management	73
B.1 Data Acquisition Infrastructure	73
B.2 Data Management Requirements	73
B.3 PyView	73
B.3.1 Overview	73
B.3.2 Instrument Management	73
B.3.3 Data Acquisition	73
B.3.4 Data Management	73
B.3.5 Data Analysis	73

C Design & Fabrication	75
C.1 Mask Design	75
C.2 Optical Lithography	75
C.3 Electron Beam Lithography	75
D Bibliography	75

List of Figures

1.1 Blueprint of a “canonical” two-qubit quantum processor	11
1.2 Circuit schematic of the realized two-qubit processor	14
1.3 Switching probabilities of the two qubit readouts as a function of the readout excitation power	15
1.4 Generating entangled two-qubit states by swapping interaction	16
1.5 Measurement of the CHSH operator of an entangled two-qubit state	18
1.6 Measured χ -matrix of the $\sqrt{i\text{SWAP}}$ gate	19
1.7 Schematic of the implementation of the Grover search algorithm	20
1.8 Measured density matrices when running the Grover algorithm	20
1.9 Single-run results of the Grover search algorithm	21
1.10 Schematic of the multi-qubit architecture realized in this thesis	22
3.1 Circuit schematic of the two-qubit processor	27
4.1 The measurement setup used for the two-qubit experiments	30
6.1 Spectroscopy of the Two-Qubit Processor	37
6.2 A qubit parameter survey showing T_1 , readout contrast and Rabi frequency of the two qubits over a large range of qubit frequencies	39
6.3 Demonstration of single-qubit IQ control	40
6.4	41
6.5 Experimentally created $ \psi_+\rangle$ ($F = 0.91$) and $ \psi_-\rangle$ ($F = 0.93$) states	41
6.6	42
6.7 test	44
6.8 The input-output density matrix of the quantum process tomography of the $\sqrt{i\text{SWAP}}$ gate. Shown are the measured density matrices of 16 different input states and the corresponding output matrices with their state fidelities. The ideal matrices are overlaid in red.	45

6.9	The input-output density matrix of the quantum process tomography of the $\sqrt{i}\text{SWAP}$ gate. Shown are the measured density matrices of 16 different input states and the corresponding output matrices with their state fidelities. The ideal matrices are overlaid in red.	46
6.10	51
7.1	Implementations of the four possible Oracle functions used in the Grover search algorithm, using only reversible gate operations	56
7.2	Full version of an implementation of the two-qubit Grover search algorithm	57
7.3	Schematic of our implementation of the Grover search algorithm	57
7.4	Pulse sequence used for implementing Grovers search algorithm	58
7.5	Quantum state tomographies at different steps during the Grover search algorithm and single-run outcome probabilities	59
7.6	Classical reversible implementation of a search algorithm on a two-bit input register. The Oracle function can be implemented by two single-bit NOT operations and a Toffoli gate. R designates the generation of a random binary value at the beginning of the algorithm If the Oracle does not yield the correct answer, the test state gets incremented. The average success probability of the algorithm is 50 %.	60
7.7	Error model used for analyzing gate and decoherence errors for the Grover search algorithm	62
7.8	Quantum state tomographies at different steps during the Grover search algorithm and single-run outcome probabilities	64
7.9	Measured single- and two-qubit readout matrices and crosstalk matrix for the Grover search algorithm experiment	65

List of Tables

7.1	Conditional probabilities $p_{ab/ uv\rangle}$ and statistical fidelities f_{ab} for all possible outcomes ab , measured for our version of Grover's algorithm.	60
7.2	Fitted gate error parameters of the Grover algorithm	63
7.3	Measured fidelities of the quantum Oracle and diffusion operators used in the Grover search algorithm	65

Chapter 1

Introduction & Summary

1.1 Quantum Computing & Circuit Quantum Electrodynamics

This thesis presents experiments performed with a superconducting two-qubit quantum processor. The main goal of this work was to demonstrate a possible quantum computing architecture based on superconducting qubits that follows the canonical blueprint of a quantum processor as shown in fig. 1.1, in accordance with the five criteria formulated by DiVincenzo (2000). By this definition, a universal quantum computer is 1.) a register of well-defined quantum bits – or qubits – 2.) with long coherence times on which one can 3) perform universal single- and two-qubit quantum gates, 4.) read out the state of each qubit individually and with high fidelity and 5.) reset the qubit register to a well-defined state.

Implementing this allegedly simple list of requirements in a system of superconducting qubits has been a major research challenge during the last decade. The first demonstration of coherent quantum-mechanical behaviour in a superconducting device was achieved by Nakamura et al. (1999) and opened up a broad research field on supercon-

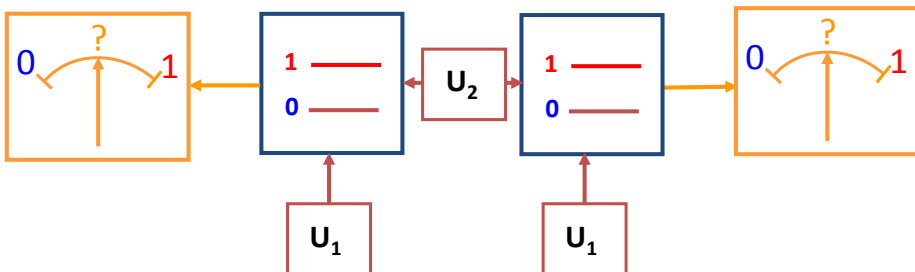


Figure 1.1: The blueprint of a “canonical” two-qubit quantum processor. Shown are two qubits that can be individually manipulated (U_1) and are connected by a universal two-qubit gate U_2 . Each of the qubits can be read out individually.

ducting quantum bits. In the years following Nakamuras initial experiment, several types of superconducting qubits were proposed and realized using e.g. the superconducting phase across a Josephson junction (Martinis et al., 1985, 2002) or the magnetic flux inside a superconducting ring interrupted by one or several Josephson junctions (Mooij et al., 1999; Chiorescu et al., 2003) as the dominant quantum variable. An important result on the way to robust superconducting qubits was the development of the so-called *Quantronium* qubit by Vion et al. (2002). The Quantronium is a Cooper pair box with comparable Josephson and charging energies operated at a well-defined “sweet spot” at which the sensitivity of the device to charge and flux noise is greatly reduced. The high coherence times achieved with the Quantronium –values larger than $2 \mu\text{s}$ have been reported– allowed for the first time the implementation of NMR-like quantum operations using a superconducting qubit (Collin et al., 2004). In 2004, the development of a new type of qubit, the so called *Transmon*, by Wallraff et al. (2004) marked again a drastic improvement in coherence times, qubit robustness and usability. The Transmon qubit is a Cooper pair box shunted with a large capacitor that drastically decreases the charging energy of the system and thus renders the device almost insensitive to charge noise but still leaves it sufficiently anharmonic to act as a qubit. With the Transmon, coherence times comparable or higher than those reported for the Quantronium have been achieved, *without* operating the qubit at a special working point, thereby greatly reducing experimental complexity. Furthermore, by embedding the Transmon qubit in a superconducting coplanar waveguide (CPW) resonator it is possible to protect it from external sources of electrical noise and to use the dispersive interaction between the qubit and the resonator for reading out the qubit state (Blais et al., 2004). This approach of embedding a superconducting qubit in a waveguide resonator has been termed –in analogy with conventional quantum electrodynamics– *circuit quantum electrodynamics* (CQED) and has gained wide popularity in the superconducting qubit community **!1!**

. So far, using this CQED approach, superconducting quantum processors with up to three qubits have been realized and two- and three-qubit quantum gates **!2!**, multi-qubit entanglement (DiCarlo et al., 2010) and simple quantum algorithms (DiCarlo et al., 2009) have been demonstrated. **!1!**

Recently, a new type of CQED architecture has been developed by Paik et al. (2011) that combines Transmon qubits with 3D cavities instead of CPW resonators, resulting again in an impressive increase of qubit coherence times of up to two orders of magnitude, with reported qubit relaxation times as high as $80 \mu\text{s}$ **!3!** and decoherence times at a comparable time scale. These drastically improved coherence times have already made possible the realization of elemental quantum feedback and error correction schemes with these systems **!4!** and make them promising candidates for the realization of a superconducting quantum computer. **!5!**

In parallel to this, the development of quantum-limited amplifiers based on nonlinear

To Do 1: add some citations of relevant experiments

To Do 2: references

Comment 1: Mention Martinis experiments with phase qubits?

To Do 3: verify this!

To Do 4: cite Irfan's paper here

To Do 5: expand this section as soon as new relevant material appears, include recent IBM, Yale

superconducting resonators by ?1? I. Siddiqi (Siddiqi et al., 2004; Vijay et al., 2009) provided a very useful tool for measuring weak quantum signals, making possible the realization of high-fidelity readout scheme for Transmon qubits (Siddiqi et al., 2006; Mallet et al., 2009). Superconducting quantum-limited amplifiers and detectors also have played a key role in the observation of quantum jumps in a superconducting qubit (Vijay et al., 2011) and in the implementation of simple quantum feedback schemes with superconducting circuits !6! .

Question 1: Should I mention Michel here?

With the research presented in this thesis we aim !2! to complement the CQED architecture as outlined in the last sections by combining a multi-qubit architecture based on Transmon qubits with a readout scheme based on quantum-limited detectors, thus providing the so-far missing per-qubit single-shot readout that would be needed to realize a canonical superconducting quantum processor with these devices.

To Do 6: Add reference to quantum feedback paper as soon as it appears

Comment 2: can I really say "we" here or should it be "I"?

The first part of the thesis discusses the realization of a superconducting two-qubit processor based on Transmon qubits fitted with individual-qubit, single-shot readouts. With this processor, we implement elementary one- and two-qubit quantum operations and use it to run a simple quantum algorithm that demonstrates probabilistic quantum speed-up. Finally, we discuss the realization of a four-qubit quantum processor using a more scalable approach that could possibly be extended to an even larger number of qubits.

1.2 Realizing a Two-Qubit Quantum Processor

The quantum processor implemented in this work is shown in fig. 1.2. It consists of two superconducting quantum bits of the Transmon-type, each equipped with its own drive and readout circuit. The qubit readout is realized using a nonlinear coplanar-waveguide resonator that serves as a *cavity bifurcation amplifier* (CBA)(Siddiqi et al., 2006; Mallet et al., 2009; Vijay et al., 2009) and allows a single-shot readout of the qubit state. Each qubit can be manipulated by driving it with microwave pulses through its readout resonator, allowing for robust and fast single-qubit operations. The qubit frequencies can be tuned individually using fast flux lines, allowing us to change the frequency of each qubit over a range of several GHz. The coupling between the two qubits is realized through a fixed capacitance that connects the two top-electrodes of the qubits and implements a fixed σ_{xx} -type qubit-qubit coupling. This coupling allows us to generate entangled two-qubit states and to implement a two-qubit gate. We use this simple processor to generate entangled two-qubit states, test the Bell inequality, implement an universal two-qubit gate and perform a simple quantum algorithm that demonstrates probabilistic quantum speed-up, as will be discussed in the following sections.

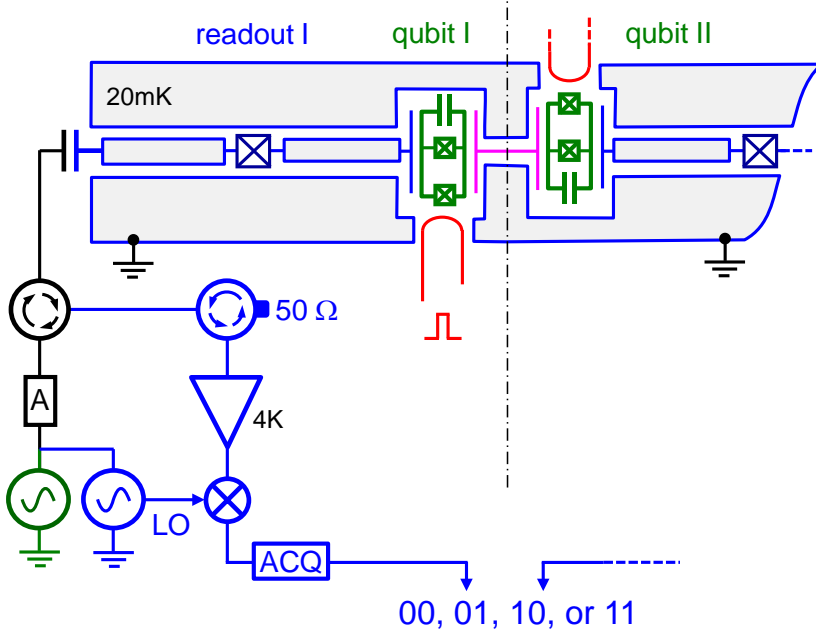


Figure 1.2: Circuit schematic of the two-qubit processor realized in this work, showing the two qubits in green, the qubit readouts in blue and the fast flux lines in red. Each qubit is embedded in its own nonlinear readout resonator and can be driven and read out through an individual microwave line.

1.3 Demonstrating Simultaneous Single-Shot Readout

To read out the state of each qubit we use a so called *cavity bifurcation amplifier* (CBA). For this readout technique, we capacitively couple the qubit to a coplanar waveguide resonator that is rendered nonlinear by placing a Josephson junction in its center conductor. The capacitive coupling between the qubit and the resonator creates a dispersive interaction between them that induces a change of the resonance frequency of the resonator dependent on the state of the qubit, and vice versa. Furthermore, the resonator can exhibit bistability at certain drive parameters due to its nonlinearity. Therefore, by driving it at a carefully chosen frequency and drive amplitude we can use the dispersive qubit-resonator interaction to map the state of the qubit to one of the bistable states of the resonator. We can then stabilize this resonator state by changing its operating point, effectively decoupling it from the further evolution of the qubit state. This allows us to measure the state of the resonator with high precision without being limited by qubit relaxation, thereby providing a high-fidelity, single-shot qubit readout. Contrary to other CQED approaches, in our setup each individual qubit is fitted with such a CBA readout, allowing hence a simultaneous readout of the full two-qubit register and following the canonical blueprint of a quantum computer as formulated by DiVincenzo. For single-qubit CBA readouts, readout fidelities up to 93 % have been reported (Mallet et al., 2009). However, due to the higher complexity and design constraints of our sys-

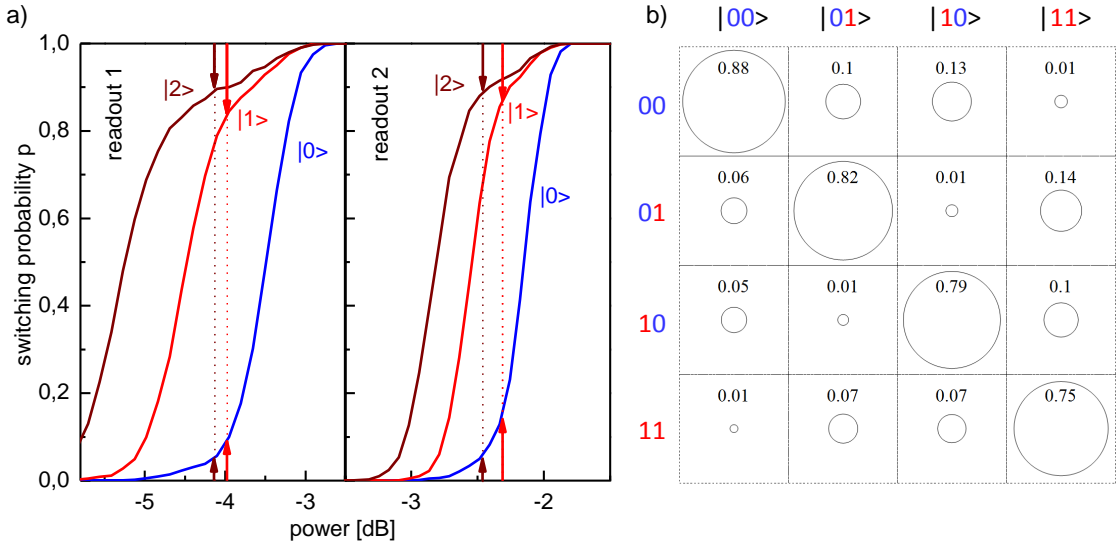


Figure 1.3: a) Switching probabilities of the two qubit readouts as a function of the readout drive power at a fixed driving frequency. The measurement is performed after preparing the qubits in the states $|0\rangle$, $|1\rangle$ and $|2\rangle$. The readout contrast is given as the difference in probability between the curves corresponding to the states $|0\rangle$ and $|1\rangle$ or $|2\rangle$, respectively. The highest contrasts of 88 and 89 % are achieved when the qubit is in state $|2\rangle$. b) Readout matrix of the two-qubit system. The matrix contains the probabilities of obtaining a given measurement result after having prepared the system in a given state. **Figure Comment 2:** Replace this figure since it is not very intuitive. It would be better to show something which allows the reader to directly quantify the visibility and readout crosstalk present in the system.

tem, only 83-89 % fidelity have been achieved for the processor presented here. The full characterization of the readout of our processor is shown in fig. 1.3. Fig. 1.3a shows the switching probabilities of each individual qubit readout as a function of the drive amplitude, measured at a fixed drive frequency. Individual curves correspond to the qubit being prepared in different states $|0\rangle$, $|1\rangle$ or $|2\rangle$, the difference between either two curves giving the readout contrast between those qubit states. Preparing the qubit in state $|2\rangle$ before readout can increase the readout fidelity by more than 10 % and is therefore often used in the experiments presented in this thesis. Fig. 1.3b shows the full readout matrix of the two-qubit register that relates measured readout switching probabilities with real qubit state occupation probabilities and allows us to correct readout errors when performing quantum state tomography.

1.4 Generating and Characterizing Entanglement

The capacitive coupling between the two qubits provides a σ_{xx} -type interaction that can be used to generate entangled two-qubit states. Conveniently, this coupling is only

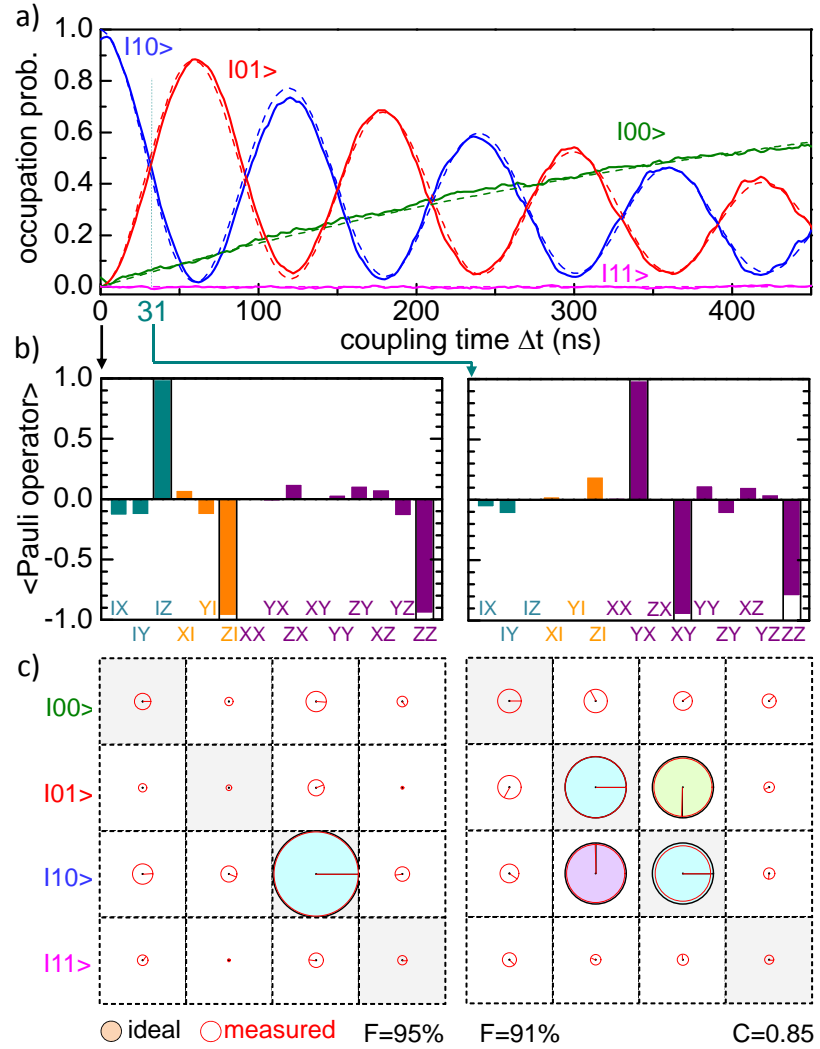


Figure 1.4: Energy oscillations between the two qubits induced by a resonant swapping interaction between them. a) The qubit state after switching on the swapping interaction for a given time Δt . The frequency of the oscillations corresponds to $2g = 8.7$ MHz. b) The Pauli set of the two-qubit state measured at 0 ns and 31 ns. c) The reconstructed density matrices corresponding to the two measured Pauli sets. In c), the area of each circle corresponds to the absolute value of each matrix element and the color and direction of the arrow give the phase of each element. The black circles correspond to the density matrices of the ideal states $|10\rangle$ and $1/\sqrt{2}/(|10\rangle + i|01\rangle)$, respectively. **Figure Comment 4: verify sign!**

effective when the qubit frequencies are near-resonant and can therefore be effectively switched on and off by tuning the qubit frequencies in and out of resonance. For the processor realized in this work, the effective coupling constant g of the two qubits has been measured as $2g = 8.2$ MHz. When the two qubits are in resonance the effective Hamiltonian of the two-qubit system can be written as

$$U(t) = \begin{pmatrix} 1 & 0 & 0 & 0 \\ 0 & \cos 2\pi t g & i \sin 2\pi t g & 0 \\ 0 & i \sin 2\pi t g & \cos 2\pi t g & 0 \\ 0 & 0 & 0 & 1 \end{pmatrix} \quad (1.1)$$

By using fast flux pulses to non-adiabatically tune the qubits in and out of resonance we can switch on this interaction for a well-defined time. We can characterize its action on the qubit register by preparing the state $|10\rangle$, tuning the qubits in resonance for a given time and measuring the qubit state afterwards. The resulting curve is shown in fig. 1.4 and clearly shows energy oscillations between the two qubits. Stopping the interaction after quarter of a period of these oscillations allows us to generate entangled Bell states that we can characterize by e.g. performing quantum state tomography. The experimental reconstruction of the density matrix of such a state corresponding to the Bell-state $|\psi\rangle = 1/\sqrt{2}(|01\rangle + i|10\rangle)$ is shown in fig. 1.4b. The measured fidelity of the prepared state of 91 % and the concurrence of 85 % confirm that entanglement is present in the system. This entanglement can also be characterized by measuring the so-called *Clauser-Horne-Shimony-Holt* operator (Clauser et al., 1969), which is given as

$$\text{CHSH} = QS + RS + RT - QT \quad (1.2)$$

with the operators Q, R, S, T being defined as

$$\begin{aligned} Q &= \sigma_z^1 & S &= \sigma_z^2 \cdot \cos \phi + \sigma_x^2 \cdot \sin \phi \\ R &= \sigma_x^1 & T &= -\sigma_z^2 \cdot \sin \phi + \sigma_x^2 \cdot \cos \phi \end{aligned} \quad (1.3)$$

Here, the angle ϕ is a parameter that should be chosen in accordance to the phase of the Bell state on which it is applied.

The expectation value $\langle \text{CHSH} \rangle$ provides a test of the quantum-mechanical character of the generated state. For classical states, the maximum value is bound by 2 but for entangled states it can reach a maximum of $\sqrt{2} \cdot 2$. Fig. 1.5 shows the result of such a CHSH-type measurement performed on a state created by the method described above, showing the value of $\langle \text{CHSH} \rangle$ as a function of the angle ϕ of the measurement basis. We observe a violation of the classical boundary 2 of the operator by 22 standard deviations when correcting the readout errors that are present in our system. The raw,

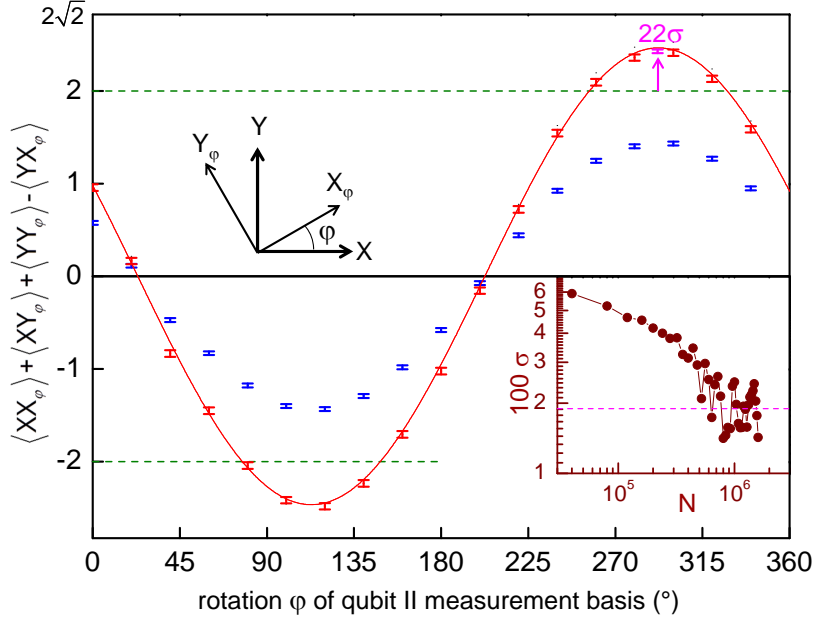


Figure 1.5: Measurement of the CHSH operator for an entangled two-qubit state. The renormalized CHSH expectation value (red points) exceeds the classical boundary of 2 by a large amount. The raw measurement data (blue points) lies below this critical threshold. The inset shows the standard deviation σ at the highest point of the curve as a function of the measurement sample size. For the highest sample count, the classical boundary is exceeded by 22 standard deviations. [Figure Comment 6: p. 140 in cavities 6 labbook](#)

uncorrected data fails to exceed the non-classical bound, making it impossible to close the detection loophole with our experiment. Nevertheless, the observed violation of the equation by the renormalized state is a strong indication of entanglement in the system.

1.5 Realizing a Universal Two-Qubit Quantum Gate

The swapping evolution given by eq. (1.1) allows not only the preparation of entangled two-qubit states but also the implementation of a two-qubit gate. When switching on the interaction for a time $t_{\pi/2} = 1/8g$ we can realize the so-called $\sqrt{i\text{SWAP}}$ gate, which has the representation

$$\sqrt{i\text{SWAP}} = \begin{pmatrix} 1 & 0 & 0 & 0 \\ 0 & 1/\sqrt{2} & i/\sqrt{2} & 0 \\ 0 & i/\sqrt{2} & 1/\sqrt{2} & 0 \\ 0 & 0 & 0 & 1 \end{pmatrix} \quad (1.4)$$

and is a universal two-qubit quantum gate. We characterize the operation and errors of our implementation of this gate by performing quantum process tomography, obtaining a gate fidelity of 90 %. The 10 % error in gate fidelity is caused mainly by qubit re-

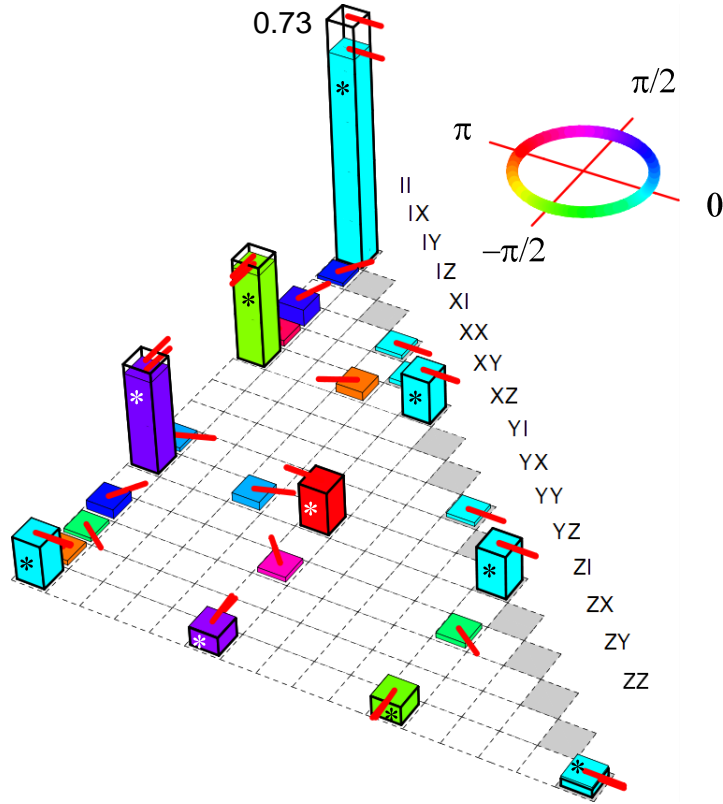


Figure 1.6: The measured χ -matrix of the implemented $\sqrt{i\text{SWAP}}$ gate. The row labels correspond to the indices of the E_i operators, the height of each bar to the absolute value of the corresponding matrix element and the color and direction of the red arrow to the complex phase of each element. The ideal χ -matrix of the $i\sqrt{\text{SWAP}}$ gate is given by the outlined bars. The upper half of the positive-hermitian matrix is not shown.

Iaxation and dephasing during the gate operation and only marginally by deterministic preparation errors, as will be discussed in the main text of the thesis. Fig. 1.6 show the measured χ matrix of the gate, which contains the full information on the quantum process describing the gate. The achieved fidelity of the gate operation is sufficient to allow the implementation of a simple quantum algorithm with our processor, as will be discussed in the following section.

1.6 Running a Quantum Search Algorithm

We can use the two-qubit quantum gate described above to run a simple quantum algorithm on our processor, the so called *Grover search algorithm* (Grover, 1997). The version of this algorithm that we implemented operates on a two-qubit basis $x_i \in \{|00\rangle, |01\rangle, |10\rangle, |11\rangle\}$ and can distinguish between four different *Oracle functions* $f(x)$ with $x \in x_i$ that each tag one given basis state x_j . The Grover algorithm for two qubits requires only one evaluation of the function $f(x)$ to determine which state has been marked and is therefore faster than any conceivable classical algorithm, which would need at most three evaluations of the Oracle function to determine it. Therefore, it demonstrates the concept of quantum speed-up in a straightforward and intuitive way. The schematic of our version of the Grover algorithm is shown in fig. 1.7 and involves

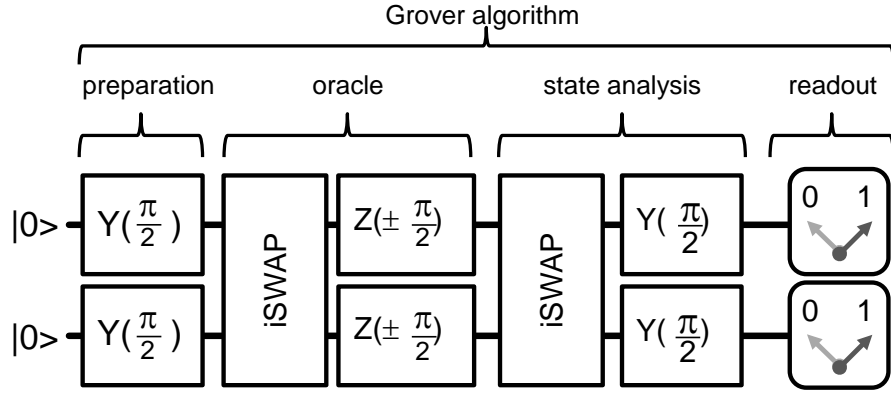


Figure 1.7: Schematic of the implementation of Grovers search algorithm on a two-qubit quantum processor. The algorithm consists in preparing a fully superposed state, applying the quantum oracle to this state and analyzing the resulting output state to determine the Oracle operator that has been applied to the state.

two *iSWAP* gate operations and six single-qubit operations along with a single-shot qubit readout at the end of the algorithm. We implemented this algorithm with our two-qubit processor and performed quantum state tomography after each step to reconstruct the quantum state at different points in the algorithm. Fig. 1.8 shows the experimentally measured density matrices when running the algorithm with an oracle that marks the state $|00\rangle$. State tomographies are shown after the first step of the algorithm (after applying a generalized Hadamard transform to the initial state $|00\rangle$), after evaluating the quantum Oracle function and after the final step of the algorithm. The measured fidelities of our implementation of the algorithm, based on the quantum state tomography of the final states for the four different Oracle functions, are 68%, 61%, 64% and 65%.

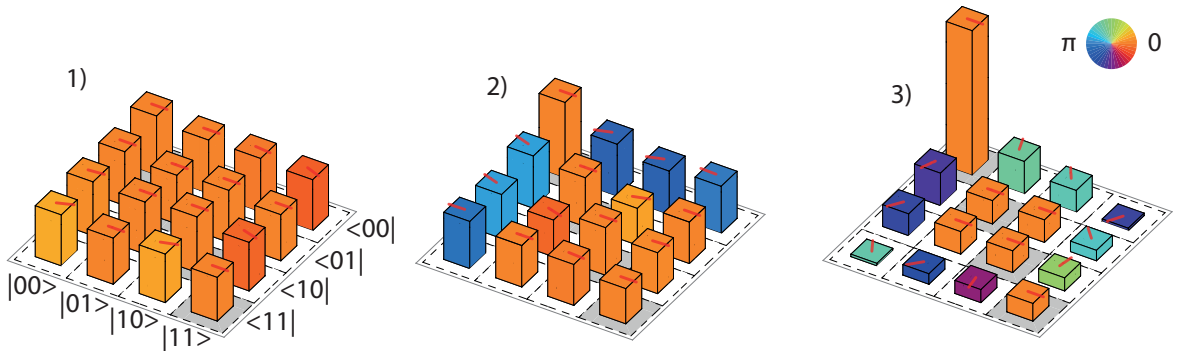


Figure 1.8: Measured density matrices when running the Grover search algorithm with a search oracle marking the state $|00\rangle$. 1) shows the state after the generalized Hadamard transform, 2) after applying the quantum oracle and 3) after the final step of the algorithm.

1.7 Demonstrating Quantum Speed-Up

The main interest of running a quantum algorithm is to obtain an advantage in the runtime in comparison to a classical algorithm, the so-called *quantum speed-up*. To characterize this quantum speed-up as obtained with our processor, we again run the Grover algorithm for all four possible Oracle functions as before, but instead of performing quantum state tomography and readout error correction, we directly read out the state of the qubit register after the last step of the algorithm *without* correcting any readout errors. When averaging the outcomes of many such individual runs of the algorithm with different Oracle functions we obtain the so-called *single-run fidelities*, which –for the four different Oracle functions– are 66%, 55%, 61% and 52%, as shown in fig. 1.9. These measured single-run fidelities clearly demonstrate the quantum speed-up in our system as compared to a classical query-and-guess algorithm, that would give the correct answer with 50% single-run fidelity. However, the achieved success probabilities are considerably lower than the theoretically possible value of 100 % , which is mainly due to relaxation and decoherence of the qubit state during the running of the algorithm and to a small degree due to errors in the pulse sequence and drifts in the measurement equipment.

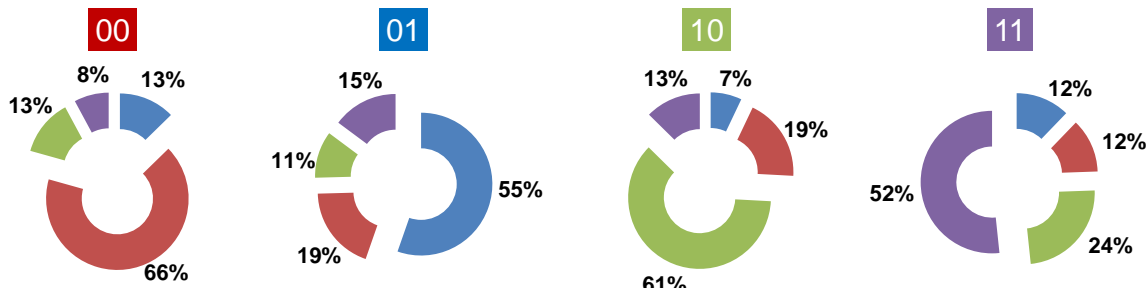


Figure 1.9: Single-run results when running the Grover search algorithm on our two-qubit quantum processor. Shown are the probabilities of obtaining the results 00, 01, 10, 11 as a function of the Oracle function provided to the algorithm, indicated by the number on top of each graph. In all four cases, the success probability of the algorithm is > 50%, thus outperforming any classical query-and-guess algorithm in the required number of calls to the Oracle function.

1.8 Designing a Scalable Quantum Computing Architecture

!3!

After having demonstrated the different building blocks of a Transmon-based quantum processor it remains to be shown that larger-scale quantum-computing beyond two

Comment 3: this section is still quite incomplete and now well-written, I have to work on the section on scalable architectures to get some more ideas

qubits is possible with such a system. In this work we therefore investigate the realization of a more scalable qubit architecture using systems of up to six qubits coupled through a so-called *quantum bus* (Majer et al., 2007). The approach for realizing a scalable quantum computing architecture pursued in this work consists of a system of many Transmon qubits equipped with individual JBA-based readouts, a multiplexed drive and readout circuit and a fixed qubit-qubit coupling mediated through a high-Q CPW resonator. As before, each qubit possesses a fluxline for fast frequency control. The readout and drive signals are send to all the qubits in parallel through a multiplexed transmission line. In this approach, the qubit and readout parameters, couplings and frequencies have to be carefully chosen to avoid unwanted coupling between individual qubits and readouts and to allow the implementation of robust quantum gates between individual qubits. In this work we realize a four-qubit chip and characterize it experimentally. The results of these experiments will be discussed in the main text of this thesis.

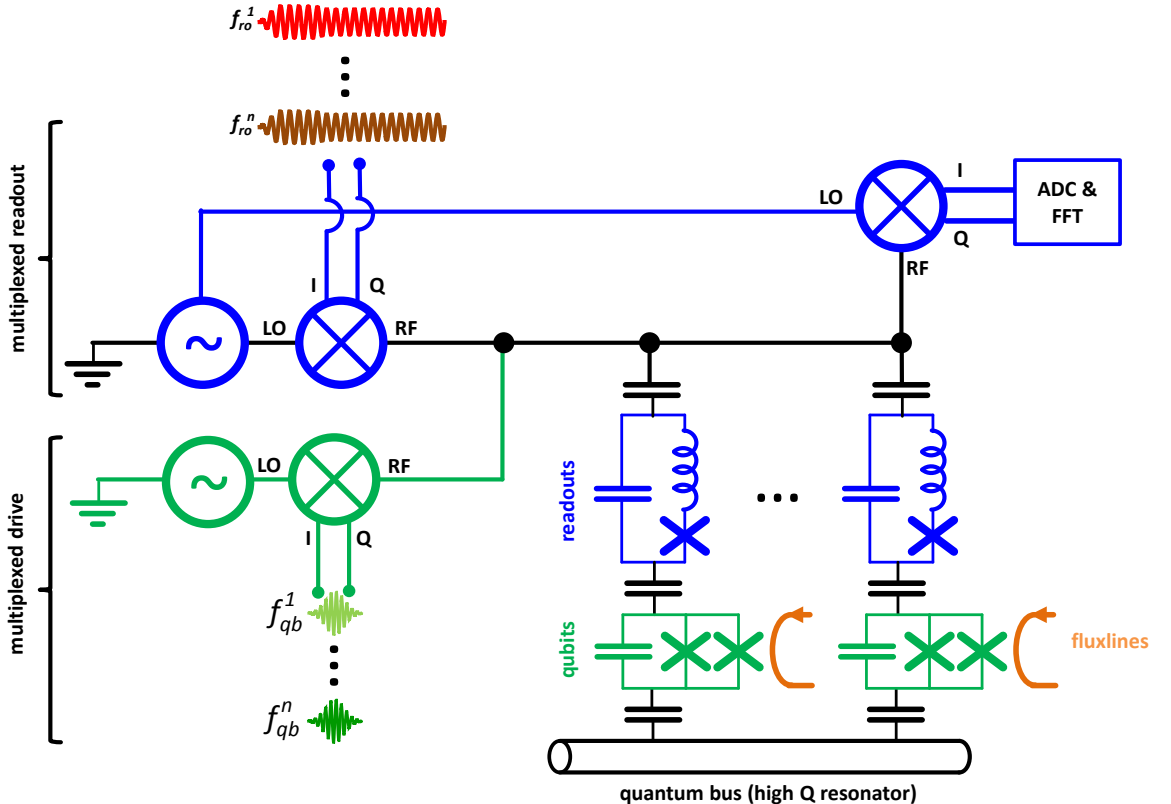


Figure 1.10: A schematic of the multi-qubit architecture realized in this thesis. Qubits and corresponding drive circuits are shown in green, JBA readouts and corresponding drive and measurement circuits in blue. Multiplexed drive and readout lines are used to manipulate and read out the qubits.

Chapter 2

Theoretical Foundations

The goal of this chapter is to provide the theoretical foundations needed to interpret and analyze the experiments discussed in the following chapters. We will therefore briefly introduce some basic concepts of quantum mechanics and quantum computing, discuss Transmon qubits and circuit quantum electrodynamics (CQED) and introduce the reader to the Josephson bifurcation amplifier that we use to read out the qubit state in our experiments. Further details on all the elements discussed here will be provided in the relevant sections of the “Experiments” chapter.

2.1 Quantum Mechanics & Quantum Computing

2.2 Transmon Qubits

A Transmon qubit is essentially a Cooper pair box (CPB) operated in the phase regime, where $E_J \gg E_C$. The Hamiltonian of the CPB can be written as (Cottet, 2002)

$$\hat{H} = 4E_C (\hat{n} - n_g)^2 - E_J \cos \hat{\phi} \quad (2.1)$$

where $E_C = e^2/C_\Sigma$ is the charging energy with $C_\Sigma = C_J + C_B + C_g$ the total gate capacitance of the system, \hat{n} is the number of Cooper pairs transferred between the islands, n_g the gate charge, E_J the Josephson energy of the junction and $\hat{\phi}$ the quantum phase across the junction.

This Hamiltonian can be solved exactly in the phase basis with the solutions being given as (Koch et al., 2007; Cottet, 2002)

$$E_m(n_g) = E_C a_{2[n_g+k(m,n_g)]}(-E_J/E_C) \quad (2.2)$$

Here, $a_\nu(q)$ denotes Mathieu's characteristic value and $k(m, n_g)$ is a function that sorts

the eigenvalues. We'll denote the energy differences between individual eigenstates by $E_{ij} = E_j - E_i$. The absolute anharmonicity of the first two Transmon transitions is given as $\alpha \equiv E_{12} - E_{01}$, the relative anharmonicity as $\alpha_r \equiv \alpha/E_{01}$. In the limit $E_J \gg E_C$ these are well approximated by $\alpha \simeq -E_C$ and $\alpha_r \simeq -(8E_J/E_C)^{-1/2}$.

2.3 Circuit Quantum Electrodynamics

For readout and noise protection, the Transmon qubit is usually coupled to a harmonic oscillator which is usually realized as a lumped-elements resonator or a coplanar waveguide resonator. In the limit where the resonator capacity $C_r \gg C_\Sigma$ we can write the effective Hamiltonian of the system as

$$\hat{H} = \hbar \sum_j \omega_j |j\rangle \langle j| + \hbar \omega_r \hat{a}^\dagger \hat{a} + \hbar \sum_{i,j} g_{ij} |i\rangle \langle j| (\hat{a} + \hat{a}^\dagger) \quad (2.3)$$

Here, $\omega_r = 1/\sqrt{L_r C_r}$ gives the resonator frequency and \hat{a} (\hat{a}^\dagger) are annihilation (creation) operators acting on oscillator states. The voltage of the oscillator is given by $V_{rms}^0 = \sqrt{\hbar \omega_r / 2C_r}$ and the parameter β gives the ratio between the gate capacitance and total capacitance, $\beta = C_g/C_\Sigma$. The coupling energies g_{ij} are given as

$$\hbar g_{ij} = 2\beta e V_{rms}^0 \langle i | \hat{n} | j \rangle = \hbar g_{ji}^* \quad (2.4)$$

When the coupling between the resonator and the Transmon is weak $g_{ij} \ll \omega_r, E_{01}/\hbar$ we can ignore the terms in eq. (2.3) that describe simultaneous excitation or deexcitation of the Transmon and the resonator and obtain a simpler Hamiltonian in the so-called *rotating wave approximation* given as

$$\hat{H} = \hbar \sum_j \omega_j |j\rangle \langle j| + \hbar \omega_r \hat{a}^\dagger \hat{a} + \left(\hbar \sum_i g_{i,i+1} |i\rangle \langle i+1| \hat{a}^\dagger + H.c. \right) \quad (2.5)$$

2.3.1 Dispersive Limit & Qubit Readout

When the qubit frequency is far detuned from the resonator frequency direct qubit-resonator transition get exponentially suppressed and the only interaction left between the two system is a dispersive shift of the transition frequencies. In this limit, the effective Hamiltonian of the system can be written as (Blais et al., 2004; Koch et al., 2007)

$$\hat{H}_{eff} = \frac{\hbar \omega'_{01}}{2} \hat{\sigma}_z + \hbar(\omega'_r + \chi \hat{\sigma}_z) \hat{a}^\dagger \hat{a} \quad (2.6)$$

Here, the resonance frequencies of both the qubit and the resonator are shifted and given as $\omega'_r = \omega_r - \chi_{12}/2$ and $\omega'_{01} = \omega_{01} + \chi_{01}$. The dispersive shift χ itself is given as

$$\chi = \chi_{01} - \chi_{12}/2 \quad (2.7)$$

$$\chi_{ij} = \frac{g_{ij}^2}{\omega_{ij} - \omega_r} = \frac{(2\beta e V_{rms}^0)^2}{\hbar^2 \Delta_i} |\langle i | \hat{n} | i+1 \rangle|^2 \quad (2.8)$$

The fact that χ_{01} and χ_{12} contribute to the total dispersive shift can cause the overall dispersive shift to become negative and even diverge at some particular working points.

2.4 The Josephson Bifurcation Amplifier

(Palacios-Laloy, 2010)

$$[L_e + L_J(i)]\ddot{q} + R_e \dot{q} + \frac{q}{C_e} = V_e \cos(\omega_m t) \quad (2.9)$$

Expanding this to second order in L_J leads to the expression

$$\left(L_e + L_J \left[1 + \frac{\dot{q}^2}{2I_0^2} \right] \right) \ddot{q} + R_e \dot{q} + \frac{q}{C_e} = V_e \cos(\omega_m t) \quad (2.10)$$

Defining the total inductance $L_t = L_e + L_J$, the participation ratio $p = L_J/L_t$, the resonance frequency $\omega_r = 1/\sqrt{L_t C_e}$ and the quality factor $Q = \omega_r L_t / R_e$ we can rewrite this as

$$\ddot{q} + \frac{\omega_r}{Q} \dot{q} + \omega_r^2 q + \frac{p \dot{q}^2 \ddot{q}}{2I_0} = \frac{V_e}{L_t} \cos(\omega_m t) \quad (2.11)$$

Chapter 3

Realizing a Two-Qubit Processor

This chapter discusses the main experimental results of this thesis. We start by discussing the implementation of a superconducting two-qubit processor, discussing the characteristics of the Transmon qubits used in the processor, the readout scheme, single-qubit manipulation, two-qubit gates as well as the experimental procedures used for quantum state and quantum process tomography. The last section of this chapter will discuss the implementation of a quantum algorithm – so called Grover search algorithm – using our two-qubit processor and the demonstration of quantum speed-up achieved with our system.

3.1 Introduction & Motivation

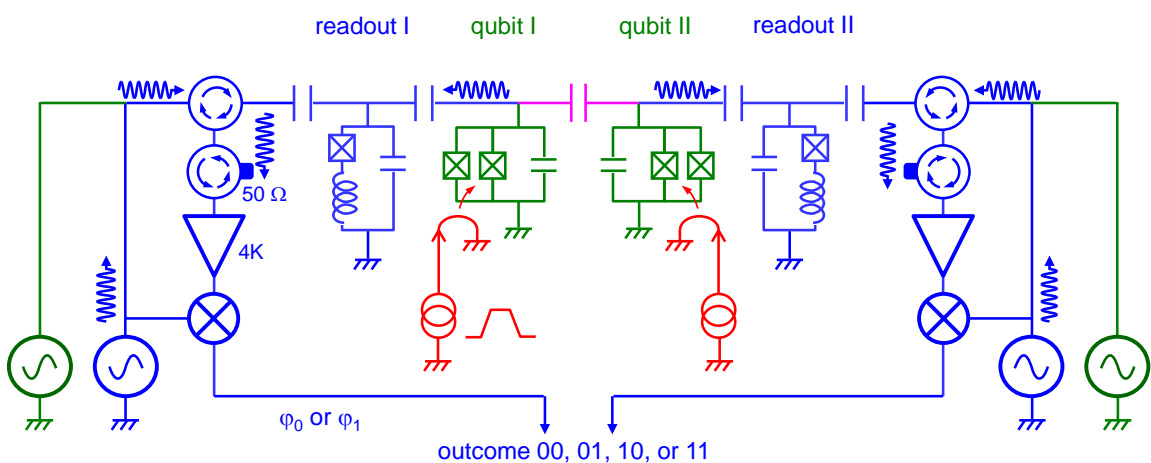


Figure 3.1: The circuit schematic of the two-qubit processor used in this work. Shown are the two Transmon qubits in green, the drive and readout circuit in blue, the fast flux lines in red and the coupling capacitance in magenta.

As discussed in the introduction, the most simple, usable quantum processor contains two qubits that are coupled by an universal two-qubit gate and which in addition

can be manipulated and read out individually. We realized such a two-qubit processor using two Transmon qubits, coupled through a fixed capacitance and readout out by individual single-shot readout of the JBA type. The circuit diagram of our processor is shown in fig. 3.1, showing the qubits, the drive and readout circuit and the coupling element between them. The following sections we'll discuss the parameters of individual parts of the processor.

3.2 Qubit Design

The parameters of the sample have been chosen in accordance to various design constraints of the qubit processor. For the qubits, the main design goals were high coherence time, good frequency tunability and fast drivability. As we will show later, the coherence time of the qubit is limited by relaxation to the ground state and coupling to external noise sources. The relaxation component of the Transmon qubit is ultimately limited by internal losses of the Josephson junction but usually is bound by coupling to the electromagnetic environment, as will be discussed later. The frequency tunability is important for the realization of fast two-qubit gates but can also limit the relaxation and coherence time of the qubit by coupling to external noise sources. The drivability speed on the other hand is limited by the anharmonicity of the qubit, which can however not be increased arbitrarily since it will make the qubit sensitive to charge noise when chosen too high. For the readout, the main design goals were readout speed and fidelity. The speed of the readout is limited by the quality factor of the readout resonator, which however also can induce qubit relaxation through the Purcell effect and may therefore not be chosen too small.

In the following paragraphs we'll therefore discuss the parameter design for our two-qubit processor and analyze the sample parameters that have been obtained.

3.3 Readout Design

3.4 Processor Fabrication

In this section we will discuss the fabrication of the two-qubit processor realized in this work.

Chapter 4

Measurement Setup

Fig. 4.1 show the measurement setup used for the two-qubit experiments. The different signal and measurement lines as well as the room-temperature and cryogenic microwave components used in our experiments will be described in the following paragraphs.

In this section we discuss the details of the measurement setup used to perform the two-qubit experiments presented in this thesis. All experiments have been performed in a custom-built dilution cryostat at $< 40 \text{ mK}$ using a cryogenic microwave signal generation and measurement chain. The individual components of this setup will be discussed in the following sections.

4.1 Sample Holder & PCB

The qubit chip is first glued to a high-frequency PCB !7! , then wirebonds are used to connect the groundplane and the center conductors of the on-chip transmission lines to their counterparts on the PCB. Finally, additional bond wires connect isolated ground planes on-chip. The realization of a good and uniform groundplane on the qubit chip and around is very important to suppress unwanted resonance modes that can be created when the connection between isolated ground planes is not good enough !8! . The mounted chip on the PCB is then placed in a Copper or Aluminium sample holder which fully encloses the PCB and serves to reduce unwanted couplings to the environment. The coplanar waveguides on the PCB are connected to Mini-SMP cables through a set of connectors that are soldered on the PCB.

To Do 7: add substrate material details

To Do 8: Add references e.g. to Schuster's thesis

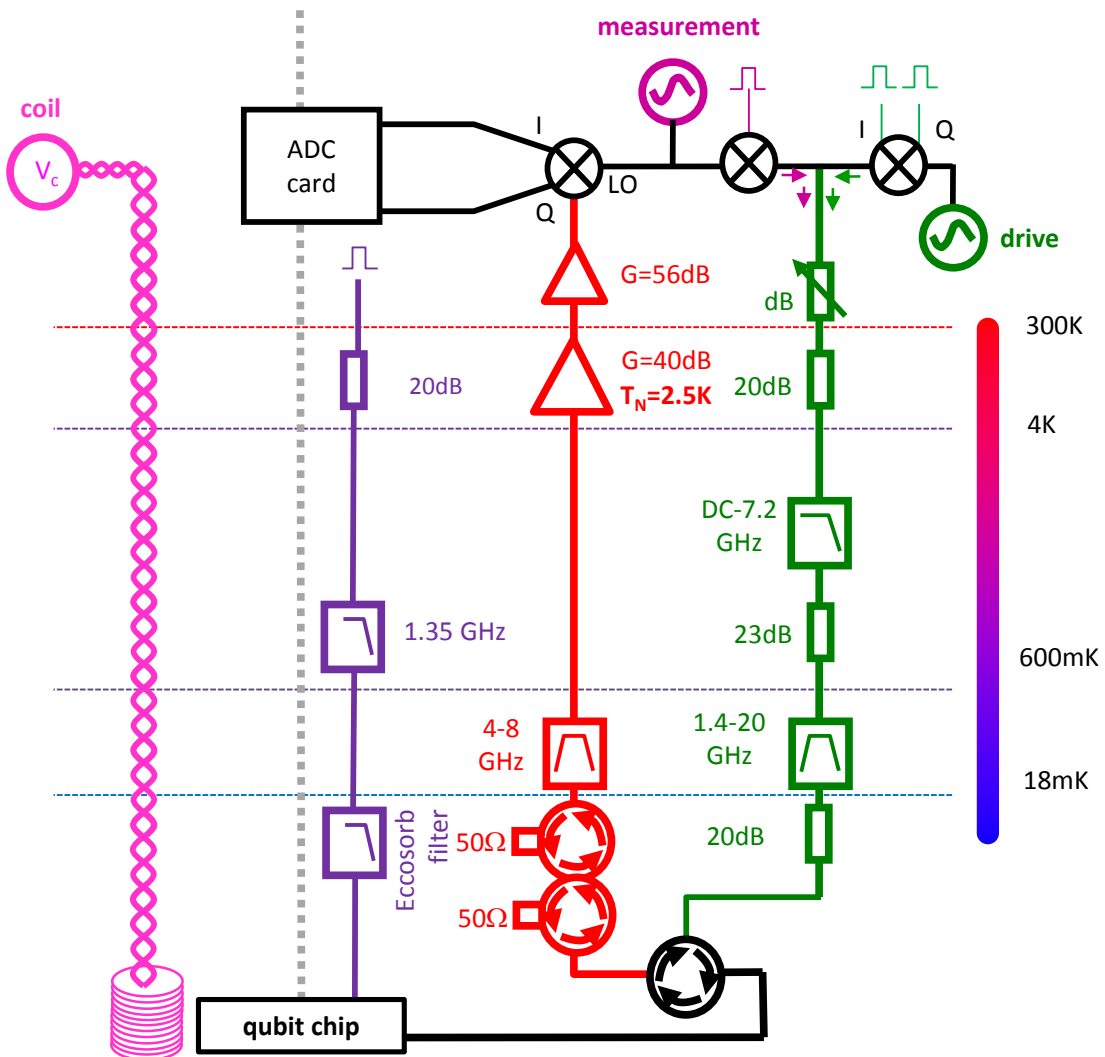


Figure 4.1: The measurement setup used for the two-qubit experiments. Exactly the same drive and readout scheme is used for both qubits with phase-locked microwave sources and arbitrary waveform generators.

4.2 Cryogenic Wiring

For the transmission of microwave signals to our sample we use various types of transmission lines suited for room-temperature and cryogenic application. The main goal of the input lines is to provide adequate signal transmission without introducing too much thermal conductance to the system. For the signal lines that carry the measurement signal from the sample we use superconducting cables [!9!](#) and low-resistance copper cables. In addition, we use superconducting bifilar cables for the DC bias of our magnetic coils. The qubit and fluxline input lines are attenuated and filtered at several stages of the cryostat to reduce signal noise.

To Do 9: add type

4.3 Signal Generation & Acquisition

Here we discuss the generation and acquisition of the different signals used to manipulate and read out our quantum processor. The experiments that have been performed require the generation, measurement and demodulation of microwave signals, the generation of fast flux control pulses and the application of DC currents to our magnetic coils.

4.3.1 Microwave Sideband Mixing

For qubit manipulation it is often advantageous to use single-sideband mixing for driving the qubit since it can provide higher ON/OFF ratios for microwave pulses and allow the driving of higher qubit-levels using a single, phase-coherent microwave source. To realize this, we use IQ mixers (Hittite !10!) that we drive with a continuous single-frequency microwave tone and two time-synchronized fast control signals generated by an arbitrary waveform generator (Tektronix AWG5014b). When feeding a signal $LO(t) = i_0 \cos(\omega_{rft}t)$ to the LO port of the mixer and two signals $I(t), Q(t)$ to the I and Q ports of the mixer one obtains a signal

$$RF(t) = I(t) \cos(\omega_{rft}t) + Q(t) \sin(\omega_{rft}t) \quad (4.1)$$

To Do 10: Add exact type number

at the LO port of the mixer. Since the IQ mixer that we use is a passive, reciprocal device one can as well feed two input signals to the LO and RF ports and obtain the demodulated signal quadratures at the I and Q ports, a technique that we'll make use of for our qubit readout scheme.

Commercially available IQ mixers often deviate from the ideal behavior as given by eq. (4.1). Typical imperfections include large insertion losses –i.e. loss of signal power between the different ports of the mixer–, RF signal leakage at zero IQ-input and frequency-dependent phase and amplitude errors of the mixed sideband signals. In order to achieve reliable single-qubit operations we need to correct the signal leakage and quadrature-specific amplitude and phase errors. The signal leakage causes a small part of the LO signal to leak through to the RF port even when the IQ inputs are zeroed. This leakage can be compensated by adding center-frequency ω_c dependent DC offset voltages to the IQ ports. The appropriate offset voltages can be determined by applying a continuous input signal at a frequency ω_c to the LO port of the mixer and minimizing the signal power at the RF port by varying the IQ offset voltages. To correct the sideband amplitude and phase errors we apply another correction procedure that we outline here. First, for the signals at the IQ inputs of the mixer we introduce the notation

$$A(t) = I(t) + iQ(t) = a(t) \exp(-i\phi(t)) \quad (4.2)$$

We consider an IQ signal at a single sideband frequency ω_{sb} and at fixed complex amplitude $a(t) = a = a_0 \exp(i\phi_0)$ such that $A(t) = a \exp(-i\omega_{sb}t)$. The effect of the gain and phase imperfections of the IQ mixers can then be modeled by assuming that the mixer adds another IQ signal $\epsilon(\omega_{sb}, \omega_c)A^*(t)$ at the mirrored sideband frequency $-\omega_{sb}$. We can correct this unwanted signal by adding a small correction $c(\omega_{sb}, \omega_c)A^*(t)$ to our IQ input signal. The correction coefficient $c(\omega_{sb}, \omega_c)$ usually depends both on the carrier frequency ω_c and the sideband frequency ω_{sb} . We determine the correction coefficients by generating a continuous waveform at a given center and sideband frequency, measuring the amplitude of the unwanted sideband signal with a fast spectrum analyzer and minimizing its amplitude by varying the correction coefficient $c(\omega_{sb}, \omega_c)$.

Both the offset and the sideband-amplitude and -phase corrections have been automatized using our data acquisition software, the resulting correction coefficients are summarized in fig. ??.

4.3.2 Fast Magnetic Flux Pulses

The fast flux lines are implemented by a pair of superconducting 50Ω transmission lines, which are attenuated by 20 dB and filtered at the 4K and 20 mK stages of the cryostat. The filtering at the 20 mK stage is realized through custom-made, highly absorptive Eccosorb filters. Fig. ?? shows an image of these filters and the attenuation characteristic obtained. The heavy filtering of the flux line greatly reduces noise seen by the qubit but also distorts all signals sent through the line. This distortion is unwanted especially at high frequencies and needs to be corrected. To do this we need to measure and compensate the frequency response of the flux line at experimental conditions. In order to do this, we feed back the flux signal sent to the sample through a transmission line which is exactly equivalent to the input line. This allows us to measure the returning signal at room temperature and – assuming symmetric distortion in the in-

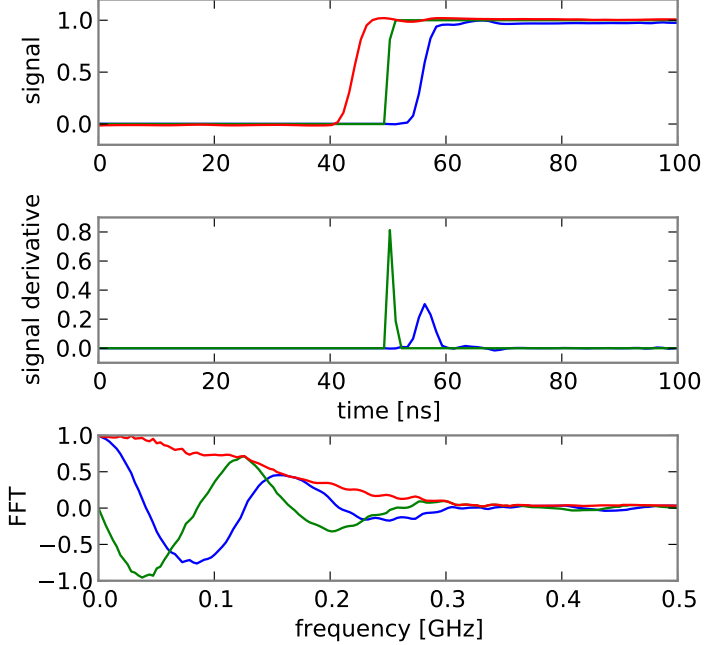


Figure 4.2: (response function filtered with a Gaussian filter with a cut-off at 0.4 GHz)

put and return line – to calculate the response function of the input line. Fig. 4.2 shows the different parts of the response function of the flux line as measured in our experiment. After eliminating the response of the analog-to-digital converter we can calculate the response function between the input port of the flux line and the sample by solving the equation

$$\dots \quad (4.3)$$

4.3.3 Pulse Synchronization

Chapter 5

Measurement Techniques

In this section we will discuss the techniques used to characterize and manipulate our two-qubit processor. All techniques employed are based on ...

5.1 Qubit Readout

5.2 Qubit Manipulation

5.3 Decoherence Time Measurement

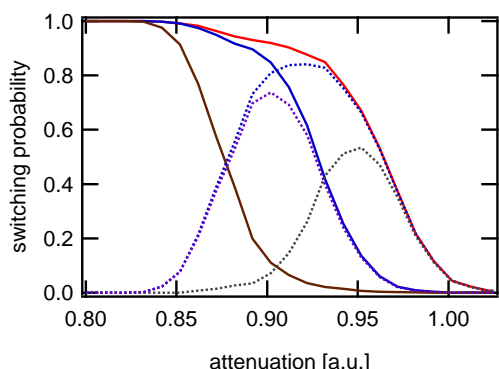


Figure 5.1: Example of a single-qubit s-curve measurement. Shown is the switching probability of the readout for a range of readout drive attenuations, for the different qubit states $|0\rangle$, $|1\rangle$ and $|2\rangle$. The difference in switching probability between individual curves defines the readout contrast between the corresponding qubit states at a given readout power attenuation.

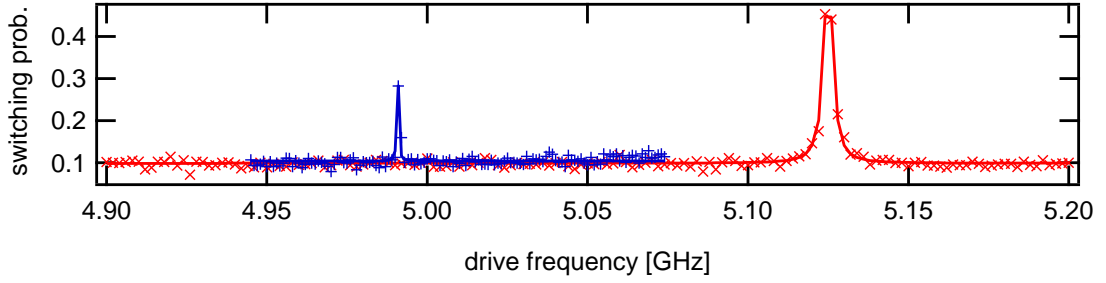


Figure 5.2: Example of a measured qubit spectroscopy. Shown is the switching probability of the qubit readout when driving the qubit with a very long drive pulse (typically $1 \mu\text{s}$) at a given drive frequency. The resonance to the right corresponds to the $|0\rangle \rightarrow |1\rangle$ (at frequency f_{01}) transition of the qubit, the resonance on the left to the 2-photon $|0\rangle \rightarrow |2\rangle$ (at frequency $f_{02}/2$) transition. We perform a Lorentzian fit of the two resonances to obtain the $|0\rangle \rightarrow |1\rangle$ and $|0\rangle \rightarrow |2\rangle/2$ resonance frequencies, from which we can calculate all other qubit transition frequencies.

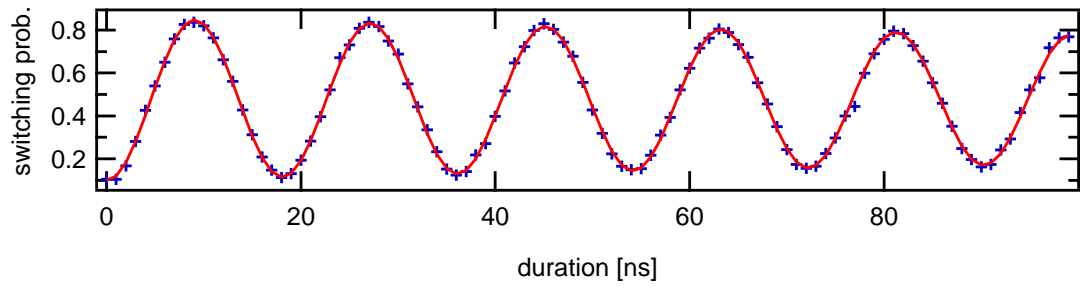


Figure 5.3: Example of a measured qubit Rabi experiment. Shown is the switching probability of the qubit readout when driving the qubit at f_{01} with a Gaussian drive pulse of varying duration. The measurement results are not corrected for readout errors.

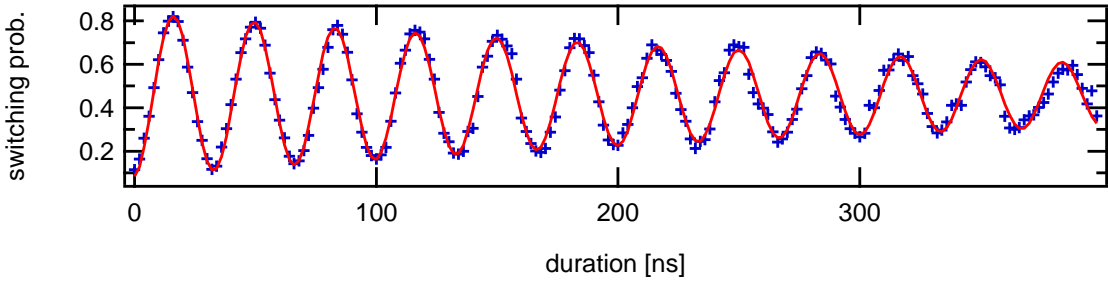


Figure 5.4: Example of a measured qubit Ramsey experiment. Shown is the switching probability of the qubit readout after performing a $X_{\pi/2}$ -wait- $X_{\pi/2}$ drive sequence at a frequency $f_{01} - \delta f$. Fitting the resulting curve with an attenuated sine-wave model allows us to determine the f_{01} frequency of the Qubit with high accuracy.

Chapter 6

Characterizing the Two-Qubit Processor

This section discusses the detailed characterization of individual circuit parts that will be used later to realize two-qubit gate and to run a quantum algorithm on the processor. The discussion will focus on the readout and microwave manipulation of the qubits as well as on the reconstruction of quantum states from measurement data, which will be used later for characterizing gate and processor operation.

6.1 Qubit & Readout Characterization

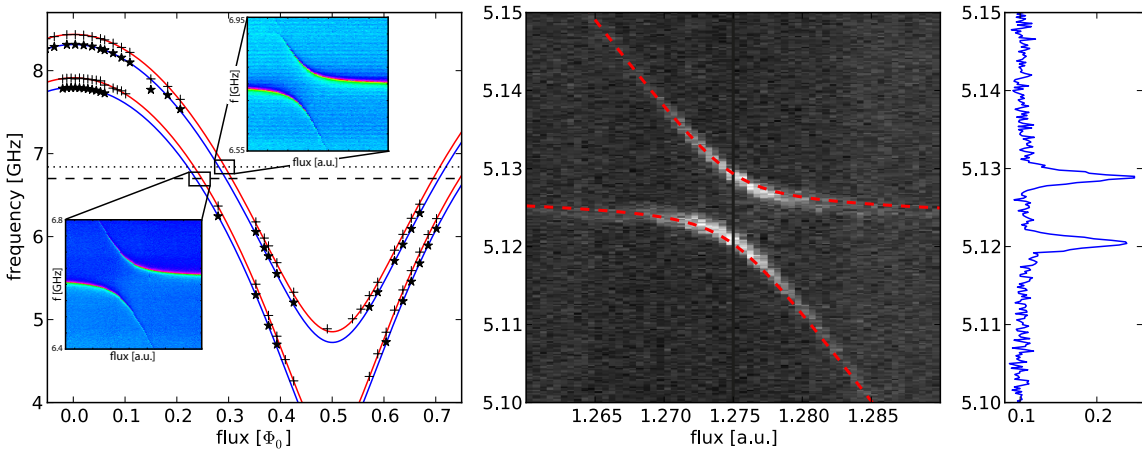


Figure 6.1: Spectroscopy of the realized two-qubit processor. a) $|0\rangle \rightarrow |1\rangle$ and $(|0\rangle \rightarrow |2\rangle)/2$ transition frequencies of the two qubits with fitted dependence and cavity frequencies. b) Avoided level crossing of the $|01\rangle$ and $|10\rangle$ levels of the qubits with fit, $g = 8.7$ MHz. c) Spectroscopy of qubit 1 at the point indicated in b).

The following section discusses the parameters of our two-qubit processor that have

been obtained by various measurements.

6.1.1 Qubit Parameters

To obtain all the relevant parameters of our two-qubit processor, we perform a set of measurements from which we obtain the qubit frequencies, anharmonicities, junction asymmetries, the inter-qubit coupling, the coupling to the microwave drive lines, the coupling of each qubit to its readout and the relaxation and dephasing times of the qubits. The drive and readout couplings as well as the relaxation and dephasing times are measured for a range of qubit frequencies, which will allow us later to pick an ideal working point for our two-qubit experiments. The qubit parameters obtained from spectroscopic measurements are as follows:

- *Qubits*: Spectroscopic measurement of the qubit transitions yielded parameter values of $E_J^I/h = 36.2$ GHz, $E_c^I/h = 0.98$ GHz and $E_J^{II}/h = 43.1$ GHz, $E_C^{II}/h = 0.87$ GHz for the Josephson and charging energies of the two qubits and values of $d^I = 0.2$, $d^{II} = 0.35$ for the qubit junction asymmetries.
- *Readout resonator*: The frequencies of the readout resonators have been measured as $\nu_R^I = 6.84$ GHz and $\nu_R^{II} = 6.70$ GHz with quality factors $Q^I \simeq Q^{II} = 730$, independent measurements of the Kerr nonlinearities yielded $K^I/\nu_R^I \simeq K^{II}/\nu_R^{II} = -2.3 \pm 0.5 \times 10^{-5}$!11! .
- *Qubit-Resonator coupling*: The coupling of the qubits to the readout resonators has been spectroscopically determined as $g_0^I \simeq g_0^{II} = 50$ MHz

To Do 11: add junction inferred parameters from the bare resonator frequencies

Readout Parameters

Qubit Readout, Driving, Relaxation and Dephasing Time

In order to obtain the relaxation time and the coupling of the qubit to the drive line, we perform an automated survey of qubit spectroscopies, qubit readout characterizations and T_1 measurements at different qubit frequencies. The results of such a parameter survey are summarized in fig 6.2, showing the relaxation time T_1 , the readout contrast c_{10} and the Rabi frequency f_{Rabi} for a fixed drive amplitude for the two qubits in a frequency range between 5.2 and 6.5 GHz. As can be seen, the relaxation time of the qubits tends to increase the farther detuned each qubit is from its readout resonator. Not surprisingly, the drive frequency of the qubit also decreases when the qubit-resonator detuning increases as expected from the Purcell effect, which filters incoming microwave signals that are far-detuned from the resonator frequency. The inverse is true for the readout contrast, which increases near-linearly when reducing the qubit-resonator detuning due

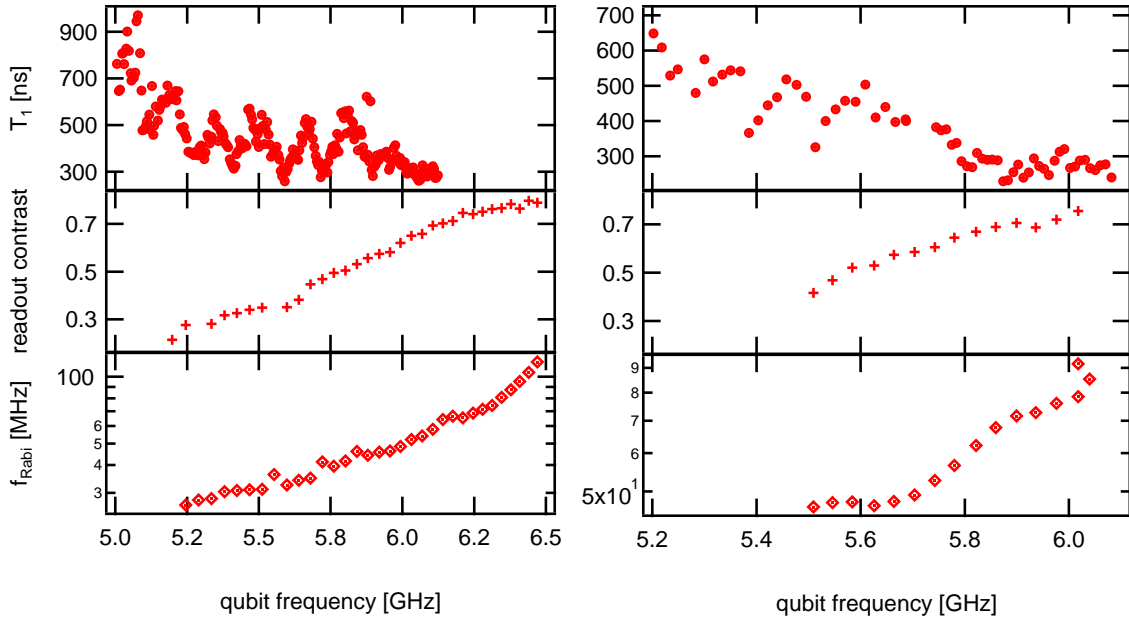


Figure 6.2: A qubit parameter survey showing the relaxation time T_1 , the readout contrast and the Rabi frequency at a fixed drive amplitude for the two qubits over a large range of qubit frequencies.

to the increase of the dispersive resonator frequency shift induced by the qubit that gets stronger the less the qubit is detuned from the readout resonator.

It is interesting to note the non-monotonous characteristic of the qubit relaxation time T_1 shown in fig. 6.2, which cannot be explained by Purcell-filtering through the readout resonator and hints at a different qubit relaxation process present in the system. A possible explanation would be the coupling of the qubit to a spurious low-Q resonance in the environment. Coupling to volumetric resonance modes of the sample holder or non-CPW resonance modes of the readout resonator can be possible explanations for the data. Also, the overall dependency of the relaxation time T_1 on the qubit-resonator detuning –ignoring the “fine-structure” present in the system– is not quadratic as would be expected from the Purcell theory but rather linear. Also, by comparing the qubit relaxation time to the Rabi drive frequency reveals that the increase in T_1 is clearly not proportional to the Purcell factor that determines the qubit relaxation rate through the readout resonator. However, the observed T_1 dependency can be partially explained by taking into account the qubit relaxation through the fast fluxline, which might be strongly-coupled to the qubit on our chip, hence inducing additional qubit relaxation beyond the Purcell and intrinsic qubit relaxation rates. This effect will therefore be studied in more detail in the following sections.

6.2 Single-Qubit Operations

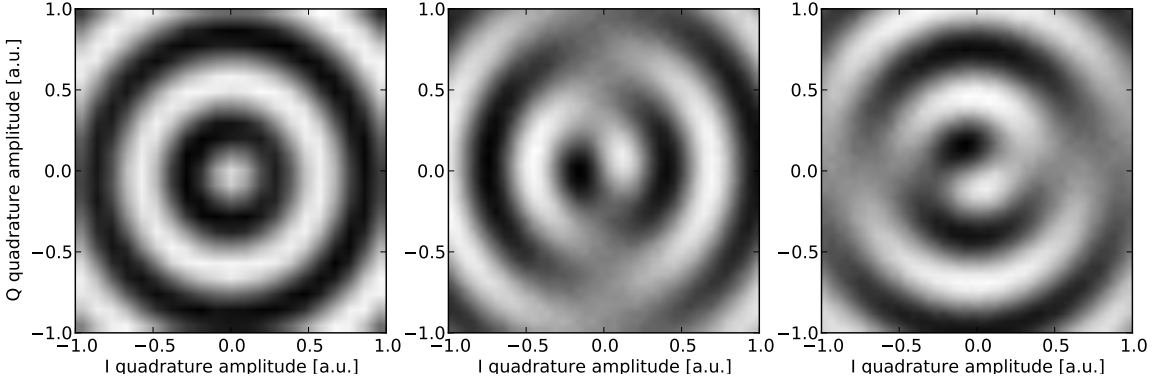


Figure 6.3: Demonstration of single-qubit IQ control. The figures show the state probability of a single qubit when preparing it in one of the states $|1\rangle$, $1/\sqrt{2}(|0\rangle+|1\rangle)$ or $1/\sqrt{2}(|0\rangle+i|1\rangle)$ and subjecting the qubit to a microwave drive pulse of the form $a(t) = V_I \cdot \cos \omega_{rf} t + V_Q \cdot \sin \omega_{rf} t$.

To perform arbitrary single-qubit operations – as needed e.g. for implementing a quantum algorithm or performing quantum state tomography – we need to implement a universal set of X , Y and Z qubit gates with our processor. Qubit rotations in the XY -plane are implemented through microwave drive pulses, where the phase of the drive pulse in reference to an arbitrary reference determines the rotation axis and the amplitude of the drive pulse the Rabi frequency of the gate. To characterize the drive pulses, we perform an experiment where we initialize a single-qubit in the states $|1\rangle$, $1/\sqrt{2}(|0\rangle+|1\rangle)$ and $1/\sqrt{2}(|0\rangle+i|1\rangle)$ and subject it afterwards to a single microwave pulse of the form $a(t) = V_I \cdot \cos \omega_{rf} t + V_Q \cdot \sin \omega_{rf} t$, which we tune by changing the input voltages V_I and V_Q to the IQ -mixer that generates the pulse from a continuous input microwave-tone at frequency ω_{rf} . We measure the qubit state at different values of V_I , V_Q , obtaining the graph shown in fig. 6.3. The qubit which was prepared in state $|1\rangle$ shows a perfectly cylinder-symmetric switching probability pattern when subjecting it to an IQ-pulse of a given phase, which is what one would expect for a qubit being prepared in either the $|0\rangle$ or $|1\rangle$ state. On the contrary, the switching probability distributions of the measured qubits prepared in the states $1/\sqrt{2}(|0\rangle+|1\rangle)$ and $1/\sqrt{2}(|0\rangle+i|1\rangle)$ are mirror-symmetric, where the switching probability does not vary at all along the drive axis which corresponds to the axis along which the qubit has been prepared. These measurements demonstrate therefore our ability to prepare and drive the qubit along arbitrary axes of the Bloch sphere. In the following sections we will analyze more in detail the drive errors inherent to our system and quantitatively analyze different error sources.

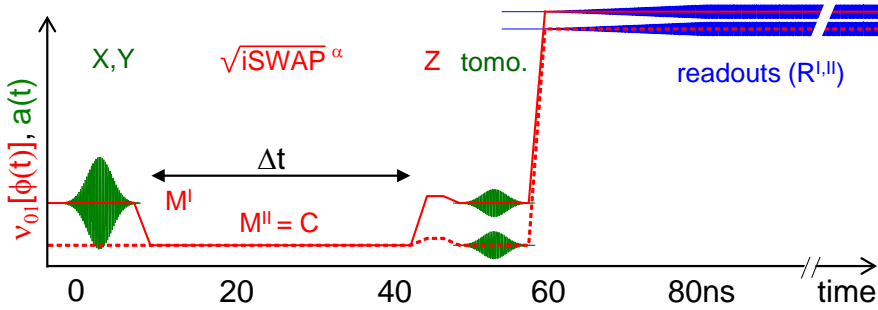
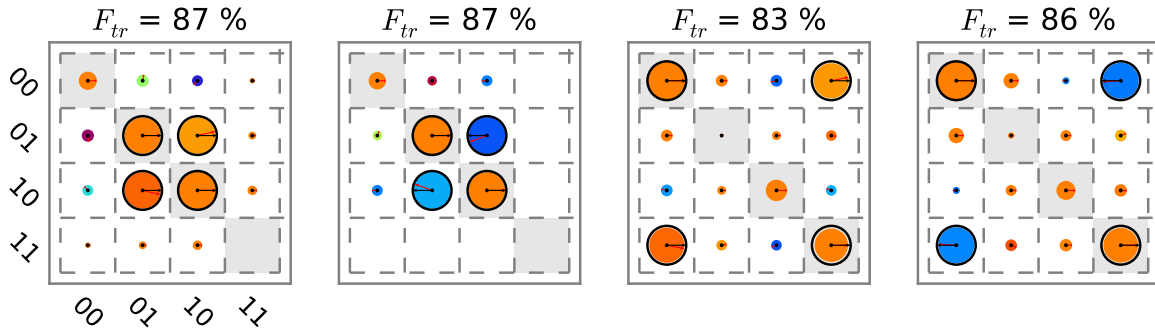


Figure 6.4

Figure 6.5: Experimentally created $|\psi_+\rangle$ ($F = 0.91$) and $|\psi_-\rangle$ ($F = 0.93$) states

6.3 Two Qubit Operations

6.3.1 Creation of Entanglement

6.3.2 Violation of the Bell Inequality

6.3.3 Quantum State Tomography of Two-Qubit States

Quantum state tomography is the procedure of experimentally determining an unknown quantum state (Michael A. Nielsen and Isaac L. Chuang, 2000).

The density matrix of an n-qubit system can be written in general form as

$$\rho = \sum_{v_1, v_2, \dots, v_n} \frac{c_{v_1, v_2, \dots, v_n} \sigma_{v_1} \otimes \sigma_{v_2} \dots \otimes \sigma_{v_n}}{2^n} \quad (6.1)$$

$$c_{v_1, v_2, \dots, v_n} = \text{tr} (\sigma_{v_1} \otimes \sigma_{v_2} \dots \otimes \sigma_{v_n} \rho) \quad (6.2)$$

where $v_i \in \{X, Y, Z, I\}$ and n gives the number of qubits in the system and where the c_{v_1, v_2, \dots, v_n} are real-valued coefficients that fully describe the given density matrix. To reconstruct the density matrix of an experimental quantum system in a well-prepared state it is therefore sufficient to measure the expectation values of these $n^2 - 1$ coefficients on an ensemble of identically prepared systems. However, statistical and systematic

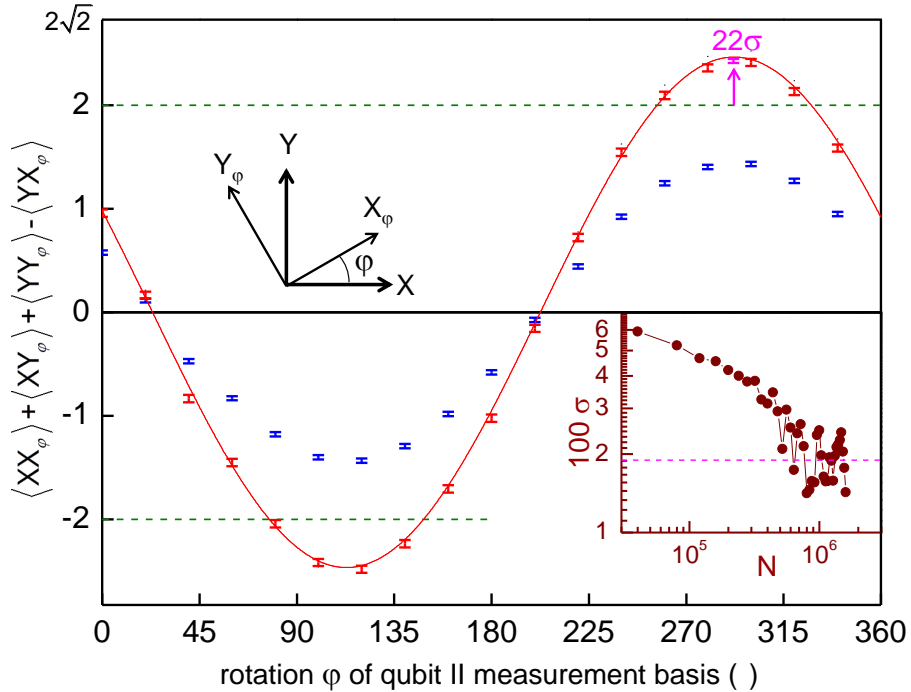


Figure 6.6

measurement errors can yield a set of coefficients that corresponds to a *non-physical* density matrix which violates either the positivity or unity-trace requirement. In the following paragraph we will therefore discuss a technique with which one can estimate the density matrix of a system in a more correct way.

Maximum Likelihood Estimation of Quantum States

A method which is often used in quantum state tomography is the so-called *maximum-likelihood* technique. Rather than directly calculating the density matrix of the system from the obtained expectation values c_{v_1, v_2, \dots, v_n} , it calculates the joint probability of measuring a set $\{c_{X, X, \dots, X}, c_{Y, X, \dots, X}, \dots, c_{I, I, \dots, I}\}$ for a given estimate of the density matrix $\hat{\rho}$. By numerically or analytically maximizing this joint probability over the set of possible density matrices we obtain the density matrix which is most likely to have produced the set of measurement outcomes that we have observed.

The joint measurement operators $\Sigma_j = \sigma_{v_1} \otimes \sigma_{v_2} \dots \otimes \sigma_{v_n}$ have the eigenvalues ± 1 and can thus be written as

$$\sigma_{v_1} \otimes \sigma_{v_2} \dots \otimes \sigma_{v_n} = |+_j\rangle\langle +_j| - |-_j\rangle\langle -_j| \quad (6.3)$$

where $|+_j\rangle$ and $|-_j\rangle$ are the eigenstates corresponding to the eigenvalues ± 1 of Σ_j .

The expectation value $\langle \Sigma_j \rangle$ can be estimated by the quantity

$$\widehat{\langle \Sigma_j \rangle}_\rho = \frac{1}{l} \sum_{i=1}^l M_i(\Sigma_j, \rho) \quad (6.4)$$

where $M_i(M, \rho)$ denotes the outcome of the i -th measurement of the operator M on the state described by the density matrix ρ . This quantity is binomially distributed with the expectation value $E(\widehat{\langle \Sigma_j \rangle}_\rho) = \langle \Sigma_j \rangle_\rho$ and the variance $\sigma^2(\widehat{\langle \Sigma_j \rangle}_\rho) = 1/l \cdot (1 - \langle \Sigma_j \rangle_\rho^2)$. For large sample sizes l , the binomial distribution can be well approximated by a normal distribution with the same expectation value and variance. The joint probability of obtaining a set of measurement values $\{s_1, \dots, s_{n^2-1}\}$ for the set of operators $\{\widehat{\langle \Sigma_1 \rangle}_\rho, \dots, \widehat{\langle \Sigma_{n^2-1} \rangle}_\rho\}$ is then given as

$$P\left(\widehat{\langle \Sigma_1 \rangle}_\rho = s_1; \dots; \widehat{\langle \Sigma_{n^2-1} \rangle}_\rho = s_{n^2-1}\right) = \prod_{i=1}^{n^2-1} \exp\left(-\frac{l}{2} \frac{(s_i - \langle \Sigma_i \rangle_\rho)^2}{1 - \langle \Sigma_i \rangle_\rho^2}\right) \quad (6.5)$$

By maximizing this probability (or the logarithm of it) we obtain an estimate of the density matrix ρ of the quantum state. This technique also allows us to include further optimization parameters when calculating the joint probability. This is useful for modeling e.g. systematic errors of the measurement or preparation process, which can be described by modifying the operators contained in the probability sum. A common source of errors in our tomography measurements are errors in the microwave pulses used to drive the qubit. Since our measurement apparatus permits us only to measure the σ_z operator of each qubit we have to perform $\pi/2$ rotations about the Y or $-X$ axes of the Bloch sphere of each individual qubit in order to measure the values of the σ_x and σ_y operators, which we therefore replace with an effective measurement of each qubits σ_z operator preceded by a rotation R_{ν_i} given as

$$R_X = \exp(-i\sigma_y\pi/4) \quad (6.6)$$

$$R_Y = \exp(+i\sigma_x\pi/4) \quad (6.7)$$

Phase and amplitude errors can be modeled as

$$R_X = \exp(-i[+\sigma_y \cos \alpha + \sigma_x \sin \alpha] [\pi/4 + \gamma]) \quad (6.8)$$

$$R_Y = \exp(+i[-\sigma_y \sin \beta + \sigma_x \cos \beta] [\pi/4 + \delta]) \quad (6.9)$$

Here, α and β represent phase errors whereas γ and δ represent amplitude errors in the drive pulses.

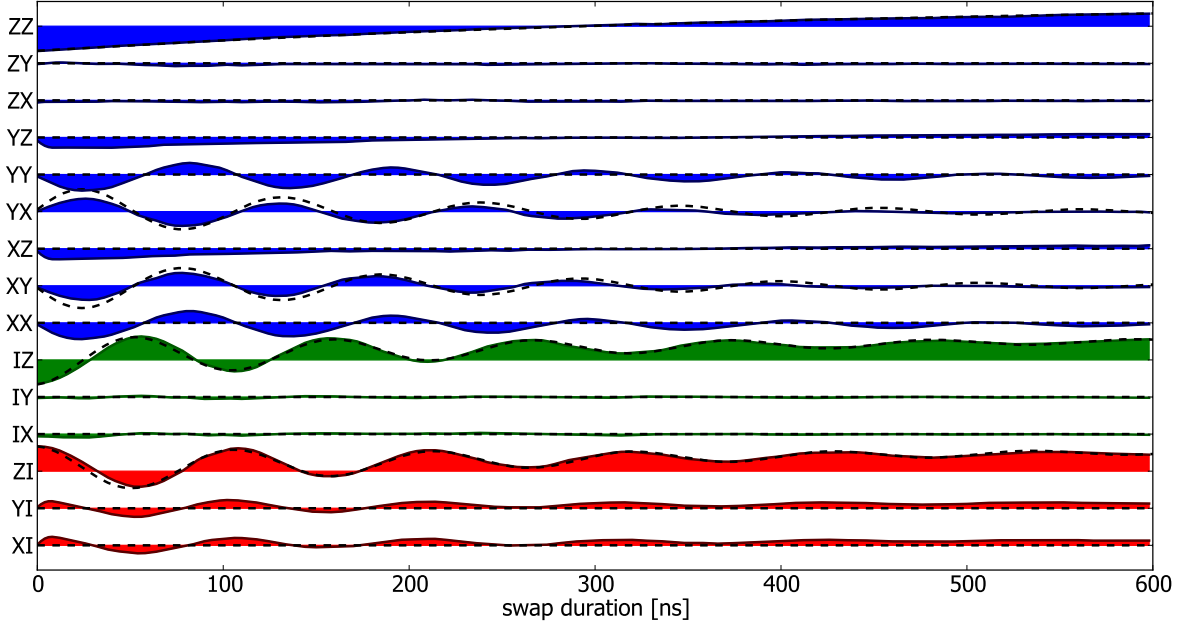


Figure 6.7: Measured Pauli operators $\sigma_i \otimes \sigma_j$ with $i, j \in \{X, Y, Z, I\}$ as a function of the interaction time. Shown are the 6 single-qubit operators as well as the 9 two-qubit correlation operators. The dashed line represents a master-equation simulation of the experiment.

6.4 Realizing a Two-Qubit Gate

6.4.1 Principle

6.4.2 Experimental Implementation

6.4.3 Quantum Process Tomography of the Gate

Introduction & Principle

Implementation

A quantum process can be described as a map $\mathcal{E} : \rho_{\mathcal{H}} \rightarrow \rho_{\mathcal{H}}$ that maps a density matrix ρ defined in a Hilbert space Q_1 to another density matrix $\mathcal{E}(\rho)$ defined in a target Hilbert space Q_2 and fulfilling three axiomatic properties Michael A. Nielsen and Isaac L. Chuang (2000); Haroche and Raimond (2006):

Axiom 6.0.1. $\text{tr} [\mathcal{E}(\rho)]$ is the probability that the process represented by \mathcal{E} occurs, when ρ is the initial state.

Axiom 6.0.2. \mathcal{E} is a *convex-linear map* on the set of density matrices, that is, for probabilities $\{p_i\}$,

$$\mathcal{E} \left(\sum_i p_i \rho_i \right) = \sum_i p_i \mathcal{E}(\rho_i) \quad (6.10)$$

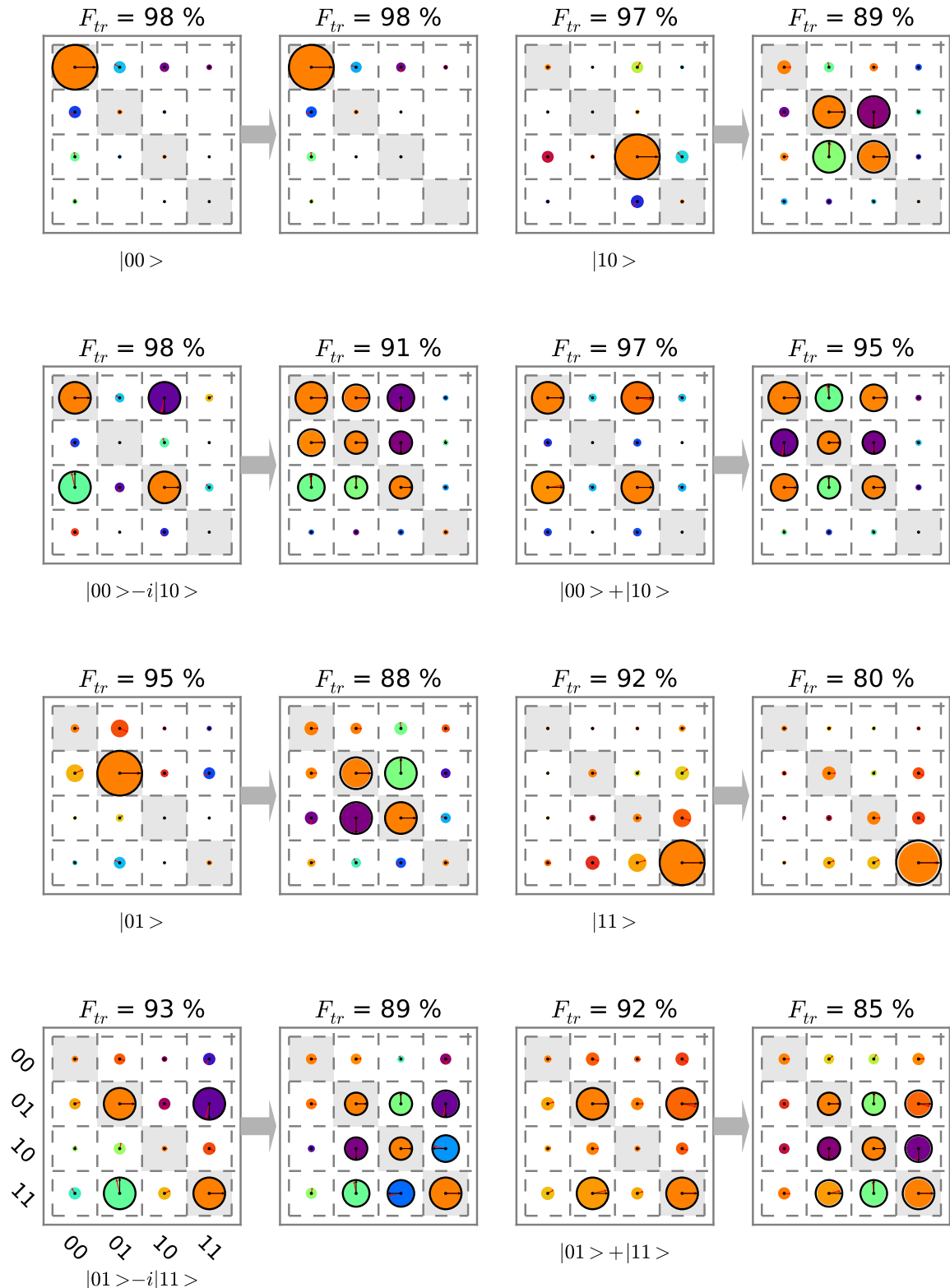


Figure 6.8: The input-output density matrix of the quantum process tomography of the $\sqrt{i\text{SWAP}}$ gate. Shown are the measured density matrices of 16 different input states and the corresponding output matrices with their state fidelities. The ideal matrices are overlaid in red.

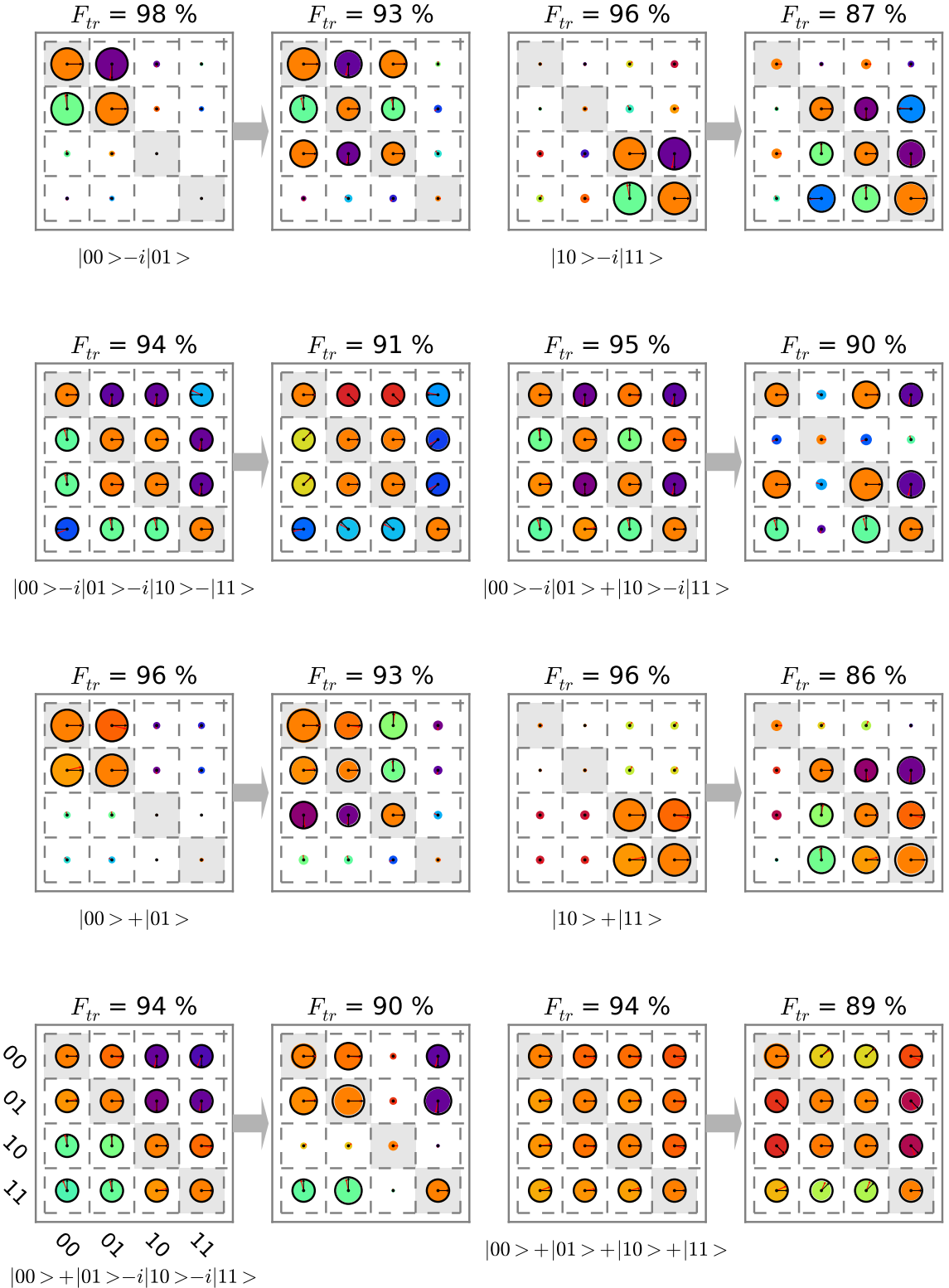


Figure 6.9: The input-output density matrix of the quantum process tomography of the \sqrt{iSWAP} gate. Shown are the measured density matrices of 16 different input states and the corresponding output matrices with their state fidelities. The ideal matrices are overlaid in red.

Axiom 6.0.3. \mathcal{E} is a *completely-positive* map. That is, if \mathcal{E} maps density operators of system Q_1 to density operators of system Q_2 , then $\mathcal{E}(A)$ must be positive for any positive operator A . Furthermore, if we introduce an extra system R of arbitrary dimensionality, it must be true that $(\mathcal{I} \otimes \mathcal{E})(A)$ is positive for any positive operator A on the combined system RQ_1 , where \mathcal{I} denotes the identity map on system R .

As shown in Michael A. Nielsen and Isaac L. Chuang (2000), any quantum process fulfilling these criteria can be written in the form

$$\mathcal{E}(\rho) = \sum_i E_i \rho E_i^\dagger \quad (6.11)$$

for some set of operators $\{E_i\}$ which map the input Hilbert space to the output Hilbert space, and $\sum_i E_i^\dagger E_i \leq I$.

Now, if we express the operators E_i in a different operator basis \tilde{E}_j such that $E_i = \sum_j a_{ij} \tilde{E}_j$ and insert into eq. (6.11), we obtain

$$\mathcal{E}(\rho) = \sum_i \sum_j a_{ij} \tilde{E}_j \rho \sum_k a_{ik}^* \tilde{E}_k^\dagger \quad (6.12)$$

$$= \sum_{j,k} \tilde{E}_j \rho \tilde{E}_k^\dagger \sum_i a_{ij} a_{ik}^* \quad (6.13)$$

$$= \sum_{j,k} \tilde{E}_j \rho \tilde{E}_k^\dagger \chi_{jk} \quad (6.14)$$

where we defined $\chi_{jk} = \sum_i a_{ij} a_{ik}^*$. This is the so-called χ -matrix representation of the quantum process. Here, all the information on the process is contained in the χ matrix, which controls the action of the process-independent operators \tilde{E}_i on the initial density matrix ρ .

Now, the goal of *quantum process tomography* is to obtain the coefficients of the χ -matrix – or any other complete representation of the process – from a set of experimentally measured density matrices ρ and $\mathcal{E}(\rho)$.

To achieve this, several techniques have been developed. The technique used in this work is the so-called *standard quantum process tomography (SQPT)*. This technique proceeds as follows:

1. Choose a set of operators E_i that forms a full basis of $\mathcal{M} : Q_1 \rightarrow Q_2$. For n-qubit process tomography we usually choose $E_{i_1, i_2, \dots, i_n} = \sigma_{i_1} \otimes \sigma_{i_2} \dots \otimes \sigma_{i_n}$, where σ_i are the single-qubit Pauli operators and $i \in \{I, X, Y, Z\}$.
2. Choose a set of pure quantum states $|\phi_i\rangle$ such that $|\phi_i\rangle \langle \phi_i|$ span the whole space of input density matrices ρ . Usually, for a n-qubit system we choose $\phi =$

$\{|0\rangle, |1\rangle, (|0\rangle + |1\rangle)/\sqrt{2}, (|0\rangle + i|1\rangle)/\sqrt{2}\}^{\otimes n}$, where \otimes^n denotes the n-dimensional Kronecker product of all possible permutations.

3. For each of the $|\phi_i\rangle$, determine $\mathcal{E}(|\phi_i\rangle \langle \phi_i|)$ by quantum state tomography. Usually we also determine $|\phi_i\rangle \langle \phi_i|$ experimentally since the preparation of this state already entails small preparation errors that should be taken into account when performing quantum process tomography.

After having obtained the ρ_i and $\mathcal{E}(\rho_i)$ one obtains the χ -matrix by writing $\mathcal{E}(\rho_i) = \sum_j \lambda_{ij} \tilde{\rho}_j$, with some arbitrary basis $\tilde{\rho}_j$ and letting $\tilde{E}_m \tilde{\rho}_j \tilde{E}_n^\dagger = \sum_k \beta_{jk}^{mn} \tilde{\rho}_k$. We can then insert into eq. (6.14) and obtain

$$\sum_k \lambda_{ik} \tilde{\rho}_k = \sum_{m,n} \chi_{mn} \sum_k \beta_{ik}^{mn} \tilde{\rho}_k \quad (6.15)$$

This directly yields $\lambda_{ik} = \sum_{m,n} \beta_{ik}^{mn} \chi_{mn}$, which, by linear inversion, gives χ .

The Kraus Representation of the Quantum Process

Besides the χ -matrix representation, there is another useful way of expressing a quantum map, the so called *Kraus representation*, which is given as

$$\mathcal{E}(\rho) = \sum_i M_i \rho M_i^\dagger \quad (6.16)$$

It can be shown (Haroche and Raimond, 2006) that this sum contains at most N elements, where N is the dimension of the Hilbert space of the density matrix ρ . We can go from the χ representation to the Kraus representation by changing the basis \tilde{E}_i such that

$$\tilde{E}_i = \sum_l a_{il} \check{E}_l \quad (6.17)$$

which, for eq. (6.14), yields

$$\mathcal{E}(\rho) = \sum_{j,k} \sum_l a_{jl} \check{E}_l \rho \sum_m a_{km}^* \check{E}_m^\dagger \chi_{jk} \quad (6.18)$$

$$= \sum_{l,m} \check{E}_l \rho \check{E}_m^\dagger \sum_{j,k} a_{jl} a_{km}^* \chi_{jk} \quad (6.19)$$

The last sum on the right side of eq. (6.19) corresponds to a change of coordinates of the matrix χ . Now, we can pick the a such that χ is diagonal in the new basis \check{E} and obtain

$$\mathcal{E}(\rho) = \sum_l \lambda_l \check{E}_l \rho \check{E}_l^\dagger \quad (6.20)$$

$$= \sum_l M_l \rho M_l^\dagger \quad (6.21)$$

with λ_l being the l -th eigenvalue of the χ matrix with the eigen-operator \check{E}_l and $M_l = \sqrt{\lambda_l} \check{E}_l$.

6.4.4 Gate Fidelity

6.4.5 Gate Error Analysis

Tomographic errors are removed from the process map of our \sqrt{iSWAP} gate using the following method. The measured Pauli sets corresponding to the sixteen input states are first fitted by a model including errors both in the preparation of the state (index *prep*) and in the tomographic pulses (index *tomo*). The errors included are angular errors $\varepsilon_{I,II}^{\text{prep}}$ on the nominal π rotations around $X_{I,II}$, $\eta_{I,II}^{\text{prep,tomo}}$ and $\delta_{I,II}^{\text{prep,tomo}}$ on the nominal $\pi/2$ rotations around $X_{I,II}$ and $Y_{I,II}$, a possible departure $\xi_{I,II}$ from orthogonality of (\vec{X}_I, \vec{Y}_I) and $(\vec{X}_{II}, \vec{Y}_{II})$, and a possible rotation $\mu_{I,II}$ of the tomographic XY frame with respect to the preparation one. The rotation operators used for preparing the states and doing their tomography are thus given by

$$\begin{aligned} X_{I,II}^{\text{prep}}(\pi) &= e^{-i(\pi+\varepsilon_{I,II}^{\text{prep}})\sigma_x^{I,II}/2}, \\ X_{I,II}^{\text{prep}}(-\pi/2) &= e^{+i(\pi/2+\eta_{I,II}^{\text{prep}})\sigma_x^{I,II}/2}, \\ Y_{I,II}^{\text{prep}}(\pi/2) &= e^{-i(\pi/2+\delta_{I,II}^{\text{prep}})[\cos(\xi_{I,II})\sigma_y^{I,II}-\sin(\xi_{I,II})\sigma_x^{I,II}]/2}, \\ X_{I,II}^{\text{tomo}}(\pi/2) &= e^{-i(\pi/2+\eta_{I,II}^{\text{tomo}})[\sin(\mu_{I,II})\sigma_x^{I,II}+\cos(\mu_{I,II})\sigma_y^{I,II}]/2}, \\ Y_{I,II}^{\text{tomo}}(-\pi/2) &= e^{+i(\pi/2+\delta_{I,II}^{\text{tomo}})[\cos(\mu_{I,II}+\xi_{I,II})\sigma_y^{I,II}-\sin(\mu_{I,II}+\xi_{I,II})\sigma_x^{I,II}]/2}. \end{aligned}$$

The sixteen input states are then $\{\rho_{\text{in}}^e = U|0\rangle\langle 0|U^\dagger\}$ with $\{U\} = \{I_I, X_I^{\text{prep}}(\pi), Y_I^{\text{prep}}(\pi/2), X_I^{\text{prep}}(-\pi/2)\} \otimes \{I_{II}, X_{II}^{\text{prep}}(\pi), Y_{II}^{\text{prep}}(\pi/2), X_{II}^{\text{prep}}(-\pi/2)\}$, and each input state yields a Pauli set $\{\langle P_k^e \rangle = \text{Tr}(\rho_{\text{in}}^e P_k^e)\}$ with $\{P_k^e\} = \{I_I, X_I^e, Y_I^e, Z_I\} \otimes \{I_{II}, X_{II}^e, Y_{II}^e, Z_{II}\}$, $X^e = Y^{\text{tomo}}(-\pi/2)^\dagger \sigma_z Y^{\text{tomo}}(-\pi/2)$, and $Y^e = X^{\text{tomo}}(\pi/2)^\dagger \sigma_z X^{\text{tomo}}(\pi/2)$. Figure S5.1 shows the best fit of the modelled $\{\langle P_k^e \rangle\}$ set to the measured input Pauli sets, yielding $\varepsilon_I^{\text{prep}} = -1^\circ$, $\varepsilon_{II}^{\text{prep}} = -3^\circ$, $\eta_I^{\text{prep}} = 3^\circ$, $\eta_{II}^{\text{prep}} = 4^\circ$, $\delta_I^{\text{prep}} = -6^\circ$, $\delta_{II}^{\text{prep}} = -3^\circ$, $\eta_I^{\text{tomo}} = -6^\circ$, $\eta_{II}^{\text{tomo}} = -4^\circ$, $\lambda_I^{\text{tomo}} = 12^\circ$, $\lambda_{II}^{\text{tomo}} = 5^\circ$, $\xi_I = 1^\circ$, $\xi_{II} = -2^\circ$, and $\mu_I = \mu_{II} = -11^\circ$.

Knowing the tomographic errors and thus $\{\langle P_k^e \rangle\}$, we then invert the linear relation $\{\langle P_k^e \rangle = \text{Tr}(\rho P_k^e)\}$ to find the 16×16 matrix B that links the vector $\overrightarrow{\langle P_k^e \rangle}$ to the columnized density matrix $\overrightarrow{\rho}$, i.e. $\overrightarrow{\rho} = B \cdot \overrightarrow{\langle P_k^e \rangle}$. The matrix B is finally applied to the measured

sixteen input and sixteen output Pauli sets to find the sixteen $(\rho_{in}, \rho_{out})_k$ couples to be used for calculating the gate map.

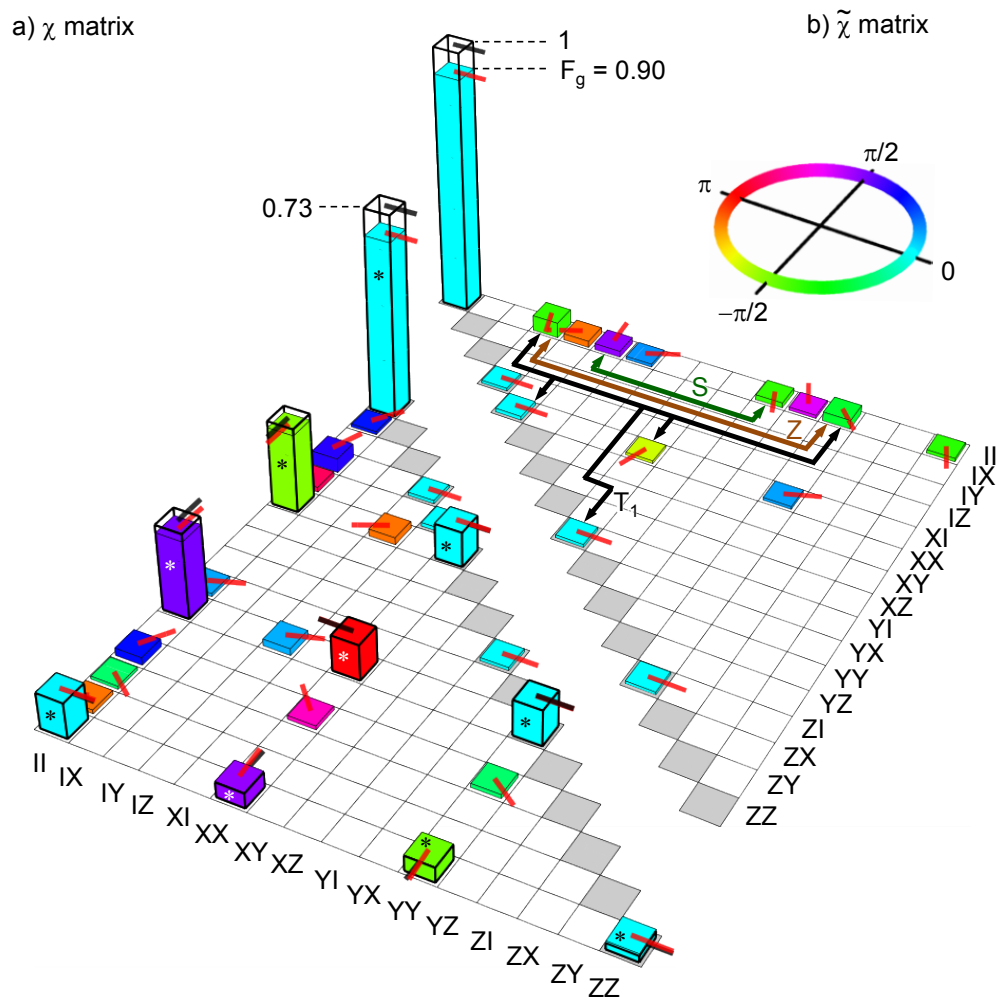


Figure 6.10

Chapter 7

Running the Grover Search Algorithm

7.1 Introduction & Motivation

The original algorithm by as given by Grover (1997) is given as follows

1. Start with the qubit register in the state $|\psi\rangle = |000\dots0\rangle$
2. Apply the Hadamard operation to the qubit register, producing the equally superposed state

$$|\psi\rangle = \frac{1}{\sqrt{n}} \sum_i^n |i\rangle$$

3. Repeat the following sequence $\mathcal{O}(\sqrt{n})$ times:

Apply the oracle operator $|i\rangle \rightarrow (-1)^{\delta_i^j} |i\rangle$ to the state $|\psi\rangle$, where $|j\rangle$ is the state marked by the oracle.

Apply the diffusion operator $|i\rangle \rightarrow -|i\rangle + \frac{2}{n} \sum_i^n |j\rangle$ to the state $|\psi\rangle$.

4. Measure the state of the quantum register

The seemingly elusive algorithm can be derived in a very clear way from Schrödinger's equation, as shown in the seminal paper by Grover (2001). Since the derivation given in this paper sheds some interesting light on the nature of the quantum search algorithm we will discuss it here. The derivation begins by considering a quantum system governed by Schrödinger's equation, which can be written as (omitting all physical constants for the sake of clarity)

$$-i\frac{\delta}{\delta t}\psi(x, t) = \frac{\delta^2}{\delta x^2}\psi(x, t) - V(x)\psi(x, t) \quad (7.1)$$

Here $\psi(x, t)$ describes the wave-function and V is a time-independent potential. Let us assume that the potential $V(x)$ is shaped as in fig. ??a, i.e. possessing a local

minimum of energy. When one initializes the system to a state $\psi_0(x, t_0)$ and lets it evolve for a given time, the resulting state $\psi(x, t)$ will have a tendency to have a high probability density in the local minimum of the potential, thus “falling” into the potential minimum much like a classical system would.

It is thus interesting to ask if one could encode the solution to some hard problem as a point of minimum energy x_0 of a potential $V(x)$ and design an algorithm that would take an initial state $\psi_0(x, t_0)$ and let it evolve into a state that has a high probability around x_0 . Most problems in classical computer science involve functions operating on binary numbers of fixed length, so to encode these numbers we can discretize our wavefunction $\psi(x, t)$ using a regular grid of points x_i with a spacing dx , as shown in fig. ??b. When we discretize the time evolution of eq. 7.1 in steps dt as well and define $\epsilon = dt/dx^2$, we obtain a new equation of the form

$$-\frac{\psi_i^{t+dt} - \psi_i^t}{dt} = \frac{\psi_{i+1}^t + \psi_{i-1}^t - 2\psi_i^t}{dx^2} - V(x_i)\psi_i^t \quad (7.2)$$

where we have written $\psi(x_i, t) = \psi_i^t$. This equation can be written in matrix form as

$$\vec{\psi}^{t+dt} = S^t \cdot \vec{\psi}^t \quad (7.3)$$

with S being a state transition matrix of the form

$$S = \begin{pmatrix} 1 - 2i\epsilon - iV(x_1)dt & i\epsilon & 0 & \dots & i\epsilon \\ i\epsilon & 1 - 2i\epsilon - iV(x_2)dt & i\epsilon & \dots & 0 \\ 0 & i\epsilon & \ddots & & \vdots \\ \vdots & & \ddots & & \vdots \\ i\epsilon & 0 & \dots & i\epsilon & 1 - 2i\epsilon - iV(x_n)dt \end{pmatrix} \quad (7.4)$$

where we have used cyclic boundary conditions and defined $\epsilon = dt/dx^2$. To calculate the wavefunction at a finite evolution time we make use the Lie-Trotter formula

$$\exp(A + B) = \lim_{N \rightarrow \infty} (\exp(A/N) \exp(B/N))^N \quad (7.5)$$

to write $\exp(S) \approx D \cdot R$ with

$$D = \begin{pmatrix} 1 - 2i\epsilon & i\epsilon & 0 & 0 & \dots & i\epsilon \\ i\epsilon & 1 - 2i\epsilon & i\epsilon & 0 & \dots & 0 \\ \dots & \ddots & & & & \vdots \\ i\epsilon & 0 & 0 & \dots & i\epsilon & 1 - 2i\epsilon \end{pmatrix} \quad (7.6)$$

and

$$R = \begin{pmatrix} e^{-iV(x_1)dt} & 0 & \dots & 0 \\ 0 & e^{-iV(x_2)dt} & \dots & 0 \\ 0 & \dots & 0 & e^{-iV(x_n)dt} \end{pmatrix} \quad (7.7)$$

This approximation is correct to $\mathcal{O}(\epsilon)$ up to an unrelevant renormalization factor. The technique of splitting up the full evolution operator into a product of two or more non-commuting evolution operators that are applied successively is widely used in digital quantum simulation (Lloyd, 1996; Lanyon et al., 2011). We can now repeatedly apply the matrix product $D \cdot R$ to the wavefunction to obtain its state after a given finite time Δt by writing

$$\vec{\psi}^{t+\Delta t} = \left(\prod_{i=1}^{\Delta t/dt} D \cdot R \right) \cdot \vec{\psi}^t \quad (7.8)$$

Using this approach, the evolution of the wavefunction is governed by two processes: The interaction of the wavefunction with the potential V and a diffusion process which mixes different spatial parts of the wavefunction. The operator D resembles a Markov diffusion process since each row and column of the matrix sums up to unity, whereas R changes the phase of each element of the wavefunction in accordance with the local potential seen by it. If we apply R to an initial state of the form $\psi_i = 1$ (we omit the normalization factor for clarity) and assume that $V_i = 0$ for $i \neq j$ and $V_j dt = \phi$, the element ψ_j will get turned according to $\psi_j \rightarrow \psi_j \exp(i\phi)$. Applying the operator D to the resulting state will transform ψ_j according to $\psi_j \rightarrow \psi_j(i + 2\epsilon(1+i))$ with a corresponding amplitude $\sqrt{1 + 4\epsilon + \mathcal{O}(\epsilon^2)}$ and the adjacent states $\psi_{j\pm 1}$ according to $\psi_{j\pm 1} \rightarrow \psi_{j\pm 1}(1 - \epsilon(1+i))$ with an amplitude $\sqrt{1 - 2\epsilon + \mathcal{O}(\epsilon^2)}$. Hence there is a transfer of amplitude between the state whose phase has been turned and its neighboring states. If we could reset the phases of the components of $\vec{\psi}$ afterwards, we would be able to iterate the application of $D \cdot R$ until all of the amplitude would have been transferred to the ψ_j . This, in essence, is what the Grover algorithm accomplishes by replacing the matrix D with an unitary matrix

$$D' = \begin{pmatrix} -1 + 2/n & 2/n & 2/n & \dots & 2/n \\ 2/n & -1 + 2/n & 2/n & \dots & 2/n \\ \vdots & & \ddots & 2/n & \vdots \\ 2/n & 2/n & 2/n & \dots & -1 + 2/n \end{pmatrix} \quad (7.9)$$

and R with an unitary matrix

$$R' = I^{n \otimes n} - 2|j\rangle\langle j| \quad (7.10)$$

where j is the index of the searched basis state. When applying $D \cdot R$ to a fully superposed state $\vec{\psi}$, a maximum amount of amplitude will be transferred to the basis state ψ_j marked by R . By repeating the $D \cdot R$ sequence $\mathcal{O}(\sqrt{n})$ times we can transfer all the amplitude into this basis state, therefore solving the search problem.

7.1.1 Ancilla-based Implementation of the Algorithm

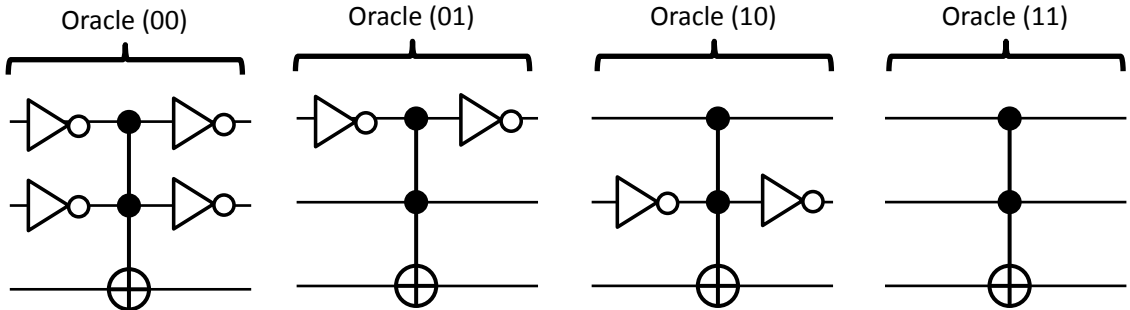


Figure 7.1: Implementations of the four possible Oracle functions used in the Grover search algorithm, using only reversible gate operations.

It is also possible to define a version of the Grover algorithm where the Oracle function does not encode the marked state directly in the input qubit register but where it uses an ancilla qubit to store the information on the marked state. Possible implementations of such ancilla-based Quantum oracle functions for the two-qubit case are shown in fig. 7.1. There, a two-qubit Toffoli gate in combination with several single-qubit NOT gates (which can be easily implemented as single-qubit X_π rotations) is used to flip the state of an ancilla-qubit conditionally on the input state of the gate. This gate is fully reversible and operates on product- as well as superposition states. Representing the quantum Oracle in this form is quite useful since it will allow us to compare the Grover algorithm with a classical search algorithm implemented using reversible gates. This will in turn allow us to compare the fidelity and success probability with that of a classical algorithm and thereby quantify the quantum speed-up achieved with our system.

Fig. 7.2 shows an implementation of the two-qubit Grover algorithm which uses the ancilla-based Oracle function. This algorithm proceeds almost identically as the compiled version which we will present in the next section, with the difference that it uses a 3-qubit control-not gate C of the form

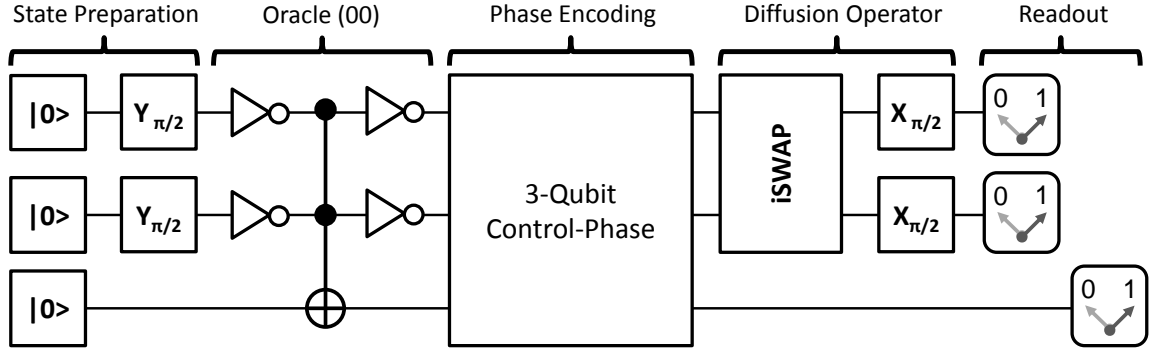


Figure 7.2: A full version of an implementation of the two-qubit Grover search algorithm. This algorithm works on a two-qubit input state and flips the state of a control qubit for one of the four possible input states in accordance to an unknown Oracle function. It then applies a 3-qubit control-phase operation of that maps $|xx1\rangle \rightarrow -|xx1\rangle$, $|xx0\rangle \rightarrow |xx0\rangle$ to encode the state of the control qubit directly in the two input qubits and then uses a diffusion operator to determine the state which has been marked by the Oracle function.

$$C = I^{n \otimes n} - 2 \sum_{ij} |ij1\rangle \langle ij1| \quad (7.11)$$

which flips the sign of all states where the ancilla qubit is in state $|1\rangle$ and hence converts the ancilla-based quantum Oracle into the phase-encoded version that was outlined before. Here, the ancilla qubit must not be read out before the two input qubits since otherwise the algorithm will fail. One can verify that the Oracle function has really marked one of the basis states by reading out the value of the ancilla qubit after having read out the other qubits and checking for a value of $|1\rangle$.

7.2 Experimental Implementation

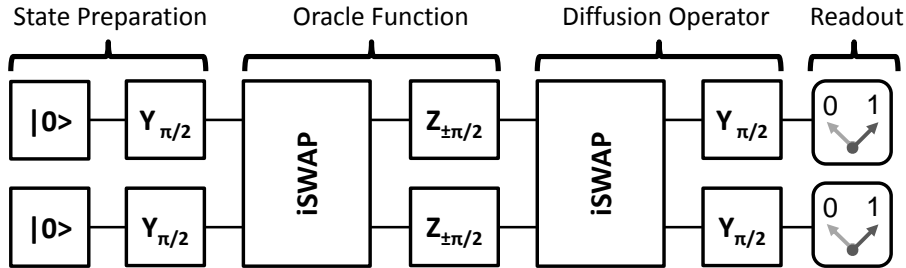


Figure 7.3: Schematic of our implementation of the Grover search algorithm. The algorithm consists in generating a fully superposed input state, applying the Oracle function to it and analyzing the resulting state by applying the Diffusion transform to it and reading out the value of the qubit register afterwards.

In this work we implement a compiled version of the two-qubit Grover algorithm. The

gate sequence of the algorithm is shown in fig. 7.3 and consists in two *iSWAP* gates and six single-qubit gates applied to an initial state $|00\rangle$. The first *iSWAP* gate together with the two single-qubit $Z_{\pm\pi}$ rotations implements the Oracle function $f(x)$ as given in eq. (7.10), where the signs of the rotation operations determines the state which is marked and can be either $|00\rangle$ (corresponding to a $Z_{-\pi/2}^1 \cdot Z_{-\pi/2}^2$ rotation), $|01\rangle$ ($Z_{-\pi/2}^1 \cdot Z_{\pi/2}^2$), $|10\rangle$ ($Z_{\pi/2}^1 \cdot Z_{-\pi/2}^2$) or $|11\rangle$ ($Z_{\pi/2}^1 \cdot Z_{\pi/2}^2$). The second *iSWAP* operation together with the following $X_{\pi/2}^1 \cdot X_{\pi/2}^2$ operation implements the diffusion operator as given by eq (7.9). The final step of the algorithm consists in reading out the two-qubit register.

7.2.1 Pulse Sequence

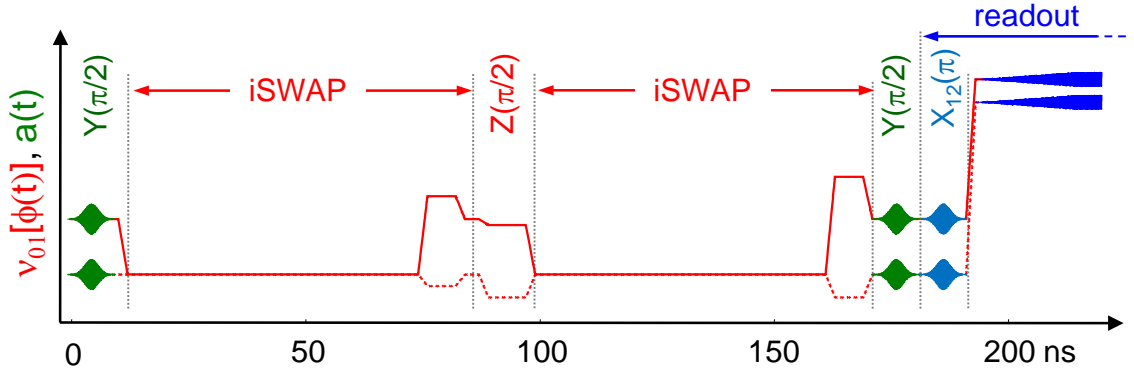


Figure 7.4: The pulse sequence used in realizing Grover's quantum search algorithm. First, a $Y_{\pi/2}$ pulse is applied to each qubit to produce the fully superposed state $1/2(|00\rangle + |01\rangle + |10\rangle + |11\rangle)$. Then, an *iSWAP* gate is applied, followed by a $Z_{\pm\pi/2}$ gate on each qubit, which corresponds to the application of the oracle function. The resulting state is then analyzed using another *iSWAP* gate and two $Y_{\pi/2}$ gates to extract the state which has been marked by the oracle function. Optionally, a Y_{π}^{12} pulse is used on each qubit to increase the readout fidelity.

7.3 Algorithm Fidelity

Likewise we can define the average fidelity of the algorithm in a single run, which corresponds to the averaged success probabilities measured for all four Oracle functions and averaged over a large sample set. Table 7.1 shows these single-run probabilities along with the so-called *user fidelities*, which are given as

$$f_{ab} = p(|ab\rangle |ab) = \frac{p(ab| |ab\rangle)}{\sum_{uv} p(uv| |uv\rangle)} \quad (7.12)$$

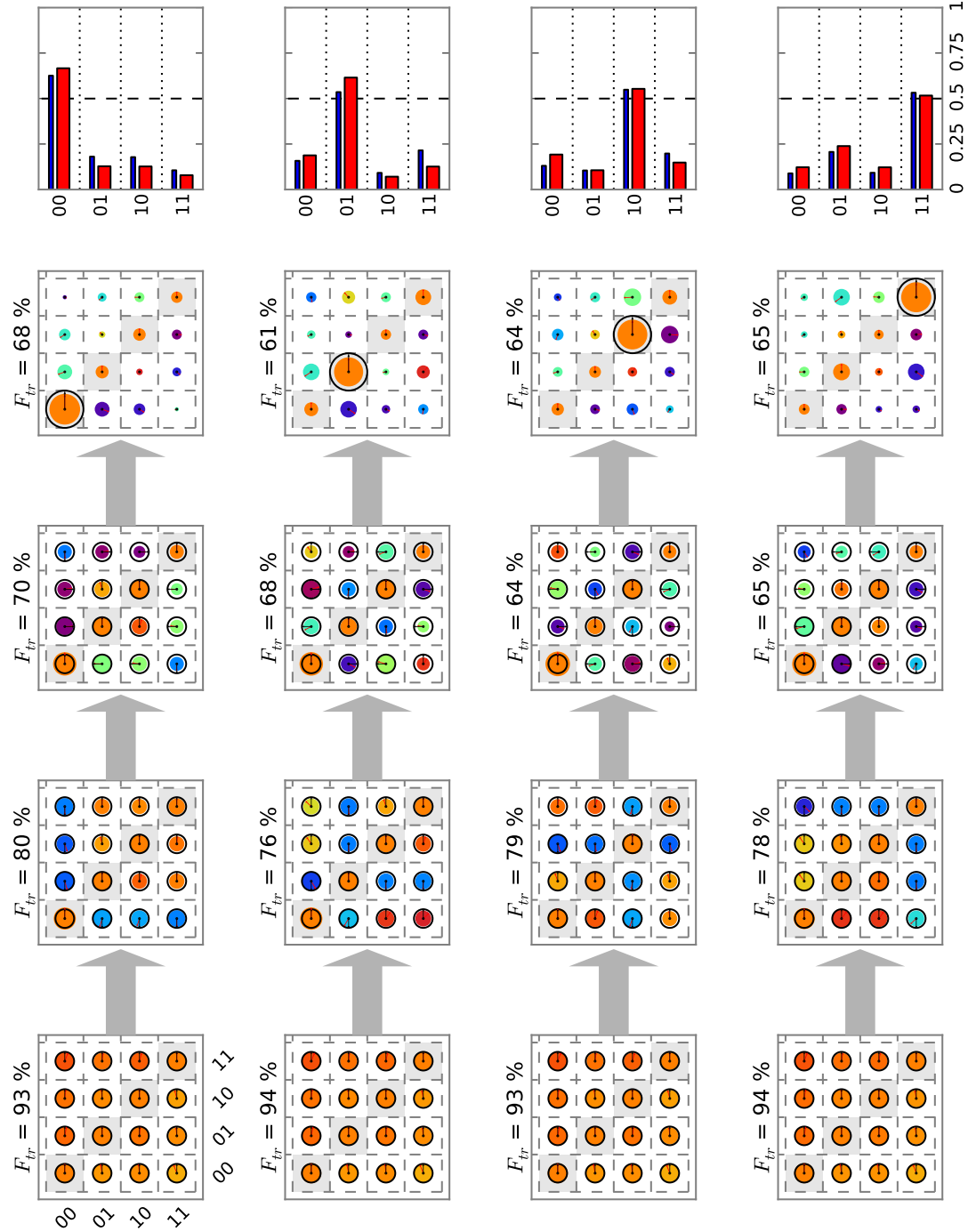


Figure 7.5: Quantum state tomographies at different steps of the Grover search algorithm and single-run outcome probabilities. The density matrices show the experimentally measured states in color and the theoretical states in black. For each state, the trace fidelity $F_{tr}(\rho_A, \rho_B) = \text{Tr}\{\rho_A \cdot \rho_B\}$ is shown above the density matrix.

and correspond to the probability of having obtained the correct answer given a certain outcome, averaged over all four possible Oracle functions. For all four, both the single-run and user fidelities are $> 50\%$, hence providing a quantum speed-up in comparision with a classical query-and-guess algorithm.

$ab/ uv\rangle$	$ 00\rangle$	$ 01\rangle$	$ 10\rangle$	$ 11\rangle$	Σ	f_{ab}
00	0.666	0.192	0.188	0.122	1.168	57.0 %
01	0.127	0.554	0.071	0.122	0.874	63.4 %
10	0.128	0.106	0.615	0.239	1.088	56.5 %
11	0.079	0.148	0.126	0.517	0.870	59.4 %

Table 7.1: Conditional probabilities $p_{ab/|uv\rangle}$ and statistical fidelities f_{ab} for all possible outcomes ab , measured for our version of Grover's algorithm.

7.4 Comparision to a Classical Algorithm

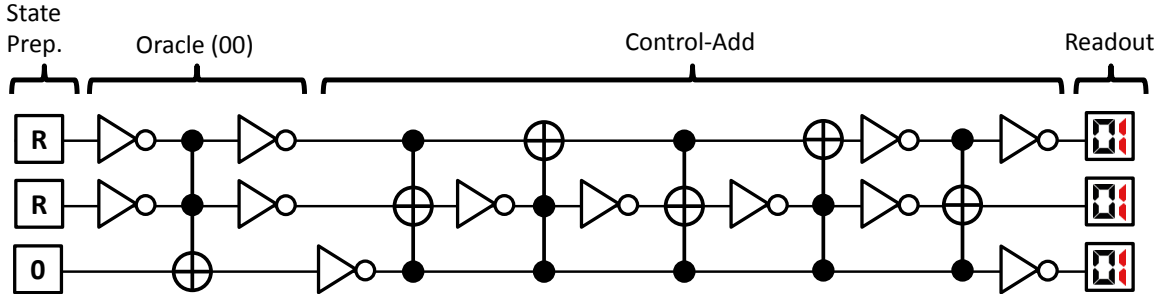


Figure 7.6: Classical reversible implementation of a search algorithm on a two-bit input register. The Oracle function can be implemented by two single-bit NOT operations and a Toffoli gate. R designates the generation of a random binary value at the beginning of the algorithm. If the Oracle does not yield the correct answer, the test state gets incremented. The average success probability of the algorithm is 50 %.

When quantifying the amount of speed-up of a quantum algorithm in comparision to a classical one, it is necessary to define a classical problem which is equivalent to the problem solved by the quantum algorithm and can be used to define a classical algorithm whose runtime can be compared to that of the quantum algorithm. For the case of the Grover search algorithm, we formulate the underlying problem in the following way:

Theorem 7.1. Given a black box $f(x)$ that works both on classical and on quantum states and takes a two-(qu)bit input value x . The black box marks one of the four possible input states x_j by flipping the state of a third control bit. We search an algorithm that returns an estimate on the value of the Oracle function that has been used inside the black box, calling the Oracle function *only once*.

7.5 Error Analysis

There are three kind of errors arising in our implementation of the Grover search algorithm which we will analyze in the following section. These errors are:

1. Deterministic, unitary gate errors arising in the algorithm
2. Stochastic errors introduced due to qubit decoherence during the runtime of the algorithm.
3. Readout errors due to qubit relaxation during the readout of the qubit state, insufficient coupling between the qubit and the readout or retrapping of the readout state during latching.

7.5.1 Gate Errors & Decoherence

Gate errors are unitary errors that arise due to misshaped or mistuned gate pulses. Usually the effect of these errors is combined with stochastic, non-unitary error sources arising due to qubit decoherence during the runtime of the algorithm. To quantify these errors we generate a model of our algorithm where we take into account both unitary as well as non-unitary error sources and perform numerical optimization of the error parameters to generate a quantitative model. We repeat this procedure for all four algorithm runs corresponding to the different Oracle functions.

Decoherence

Usually we can model decoherence processes in our algorithm either by integrating an effective master equation. For our error model, however, we chose to use a set of discrete decoherence operators that model amplitude (i.e. T_1) and phase damping (i.e. T_ϕ) processes. We can model the decoherence in our algorithm by applying these operators to the calculated quantum states after each individual step of the algorithm, taking into account the experimental runtime of the step. By this we can generate an error model incorporating the most relevant experimental decoherence processes without needing to numerically integrate a Lindblad equation, thereby greatly speeding up the parameter fitting.

The single-qubit operators describing amplitude-damping (i.e. energy relaxation) of the qubit state are given as (Michael A. Nielsen and Isaac L. Chuang, 2000)

$$E_1^{T_1} = \begin{pmatrix} 1 & 0 \\ 0 & \sqrt{1 - \gamma_{T_1}} \end{pmatrix} \quad E_2^{T_1} = \begin{pmatrix} 0 & \sqrt{\gamma_{T_1}} \\ 0 & 0 \end{pmatrix} \quad (7.13)$$

The phase-damaging (i.e. dephasing) operators can be written as

$$E_1^{T_{\phi 1}} = \begin{pmatrix} 1 & 0 \\ 0 & \sqrt{1 - \gamma_{\phi}} \end{pmatrix} \quad E_2^{T_{\phi 1}} = \begin{pmatrix} 0 & 0 \\ 0 & \sqrt{\gamma_{\phi}} \end{pmatrix} \quad (7.14)$$

Both operators are applied to ρ according to

$$\rho \rightarrow E_1 \rho E_1^\dagger + E_2 \rho E_2^\dagger \quad (7.15)$$

and result in a trace-preserving, non-unitary evolution of the quantum state of ρ . The decoherence factors γ in the operators can be calculated from the corresponding relaxation and dephasing rates as $\gamma_{T_{1,2}}(t) = 1 - \exp(-t\Gamma_{1,2})$ and $\gamma_{\phi_{1,2}} = 1 - \exp(-t\Gamma_{1,2}^{T_{\phi}}/2)$, where t is the time during which the state is exposed to the decoherence process.

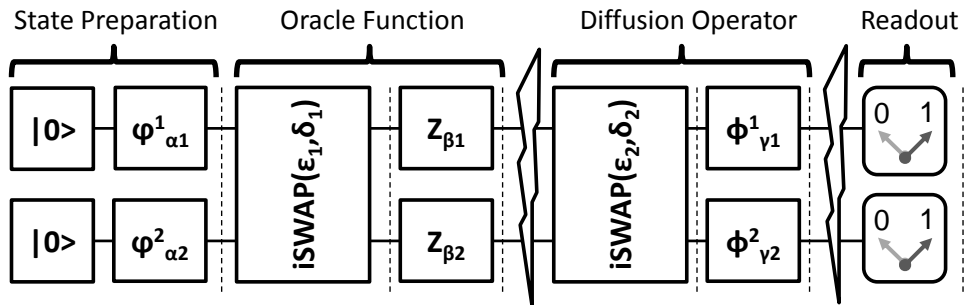


Figure 7.7: The error model we use to analyze the different gate and decoherence errors present when running the Grover search algorithm. The dotted lines indicate the points at which the quantum state has been measured by state tomography. Zigged arrows indicate the decoherence present in the system.

The full error model that we use to model the algorithm is shown in fig. 7.7. In this model, we take into account the following errors

- **Energy relaxation and phase decoherence:** We model energy relaxation and phase relaxation of our qubit by using the processes given in eqs. (7.13) and (7.14), applying the energy relaxation operator after each step of the algorithm, taking into account gate time of the performed operation.
- **Single-qubit gate errors:** We model rotation angle and rotation phase errors of our single-qubit X_α and Y_α gates by replacing them with operators of the form $X_\alpha \rightarrow \phi_{\alpha'} = \cos \phi X_{\alpha'} + \sin \phi Y_{\alpha'}$ and $Y_\alpha \rightarrow \varphi_{\alpha'} = \sin \varphi X_{\alpha'} + \cos \varphi Y_{\alpha'}$. For Z -type single-qubit operators we model only rotation angle errors by replacing $Z_\alpha \rightarrow Z_{\alpha'}$.
- **Two-qubit gate errors:** We model both detuning and gate-length errors of our $i\text{SWAP}$ 2-qubit gates.

The evolution operator of a detuned iSWAP operation is given as

$$i\text{SWAP}(t, \Delta) = \begin{pmatrix} 1 & 0 & 0 & 0 \\ 0 & \cos t g_e - i \frac{\Delta}{g_e} \sin t g_e & i \frac{g}{g_e} \sin t g_e & 0 \\ 0 & i \frac{g}{g_e} \sin t g_e & \cos t g_e + i \frac{\Delta}{g_e} \sin t g_e & 0 \\ 0 & 0 & 0 & 1 \end{pmatrix} \quad (7.16)$$

where $g_e = \sqrt{g^2 + \Delta^2}$ is the effective swap frequency at a qubit frequency detuning $f_{01}^1 - f_{01}^2 = 2\Delta$. Often it is practical to replace t and Δ with $\beta = t g_e$ and $\delta = \Delta/g$. Using this notation of the iSWAP gate and the definition of the single-qubit gates as discussed before, the full algorithm with gate errors can be written as (for right-multiplication)

$$\text{Grover} = \phi_{\gamma_1}^1 \otimes \phi_{\gamma_2}^2 \cdot i\text{SWAP}(\epsilon_2, \delta_2) \cdot Z_{\beta_1} \otimes Z_{\beta_2} \cdot i\text{SWAP}(\epsilon_1, \delta_1) \cdot \varphi_{\alpha_1}^1 \otimes \varphi_{\alpha_2}^2 \quad (7.17)$$

In addition, we add a dephasing and relaxation error after each step of the algorithm to simulate the decoherence during the executing. Numerical optimization is used to produce a fit of all the gate error parameters, which is shown in tab. 7.2. The qubit relaxation and dephasing times have been measured independently and are not part of the fit.

state	δ_1	δ_2	α_1	α_2	φ_1	φ_2	ϵ_1	β_1	β_2	ϵ_2	γ_1	γ_2	ϕ_1	ϕ_2
$ 00\rangle$	0.06	-0.06	-2.5	2.7	6.1	3.1	-7.3	-3.3	-4.1	7.5	29	9.3	0.66	-1.7
$ 01\rangle$	0.04	-0.3	-0.1	0.1	7.9	3.6	-11	-5.9	2.2	-6.9	28	-19	9	2
$ 10\rangle$	0.09	-0.2	-3.1	1.7	1	-2.5	-6.5	-15	-22	-7.5	-15	32	3.6	5.2
$ 11\rangle$	0.16	0.13	-6	3.9	2.2	0.9	-9.5	-20	-15	17	-12	-32	-7	-8.9

Table 7.2: Fitted error parameters for the measured density matrices, modeled according to the error model given in eq. (7.17). All angles are given in deg.

Fig. 7.8 shows again the measured density matrices for our realization of the Grover search algorithm, this time overlaid with the numerically optimized error model according to eq. (7.17). As can be seen, our error model is able to capture most of the observed experimental errors and to reproduce to a very good accuracy the observed density matrices. The state fidelity according to eq. ?? is shown above each density matrix and is higher than 98 % on average.

Fidelity of the Oracle and diffusion operators

It is interesting to analyze the individual fidelity of the Oracle and diffusion operators that make up the Grover algorithm. For this, we compare the action of the ideal operators D' and R' with that of the experimentally implemented versions D'_e and R'_e , taking the

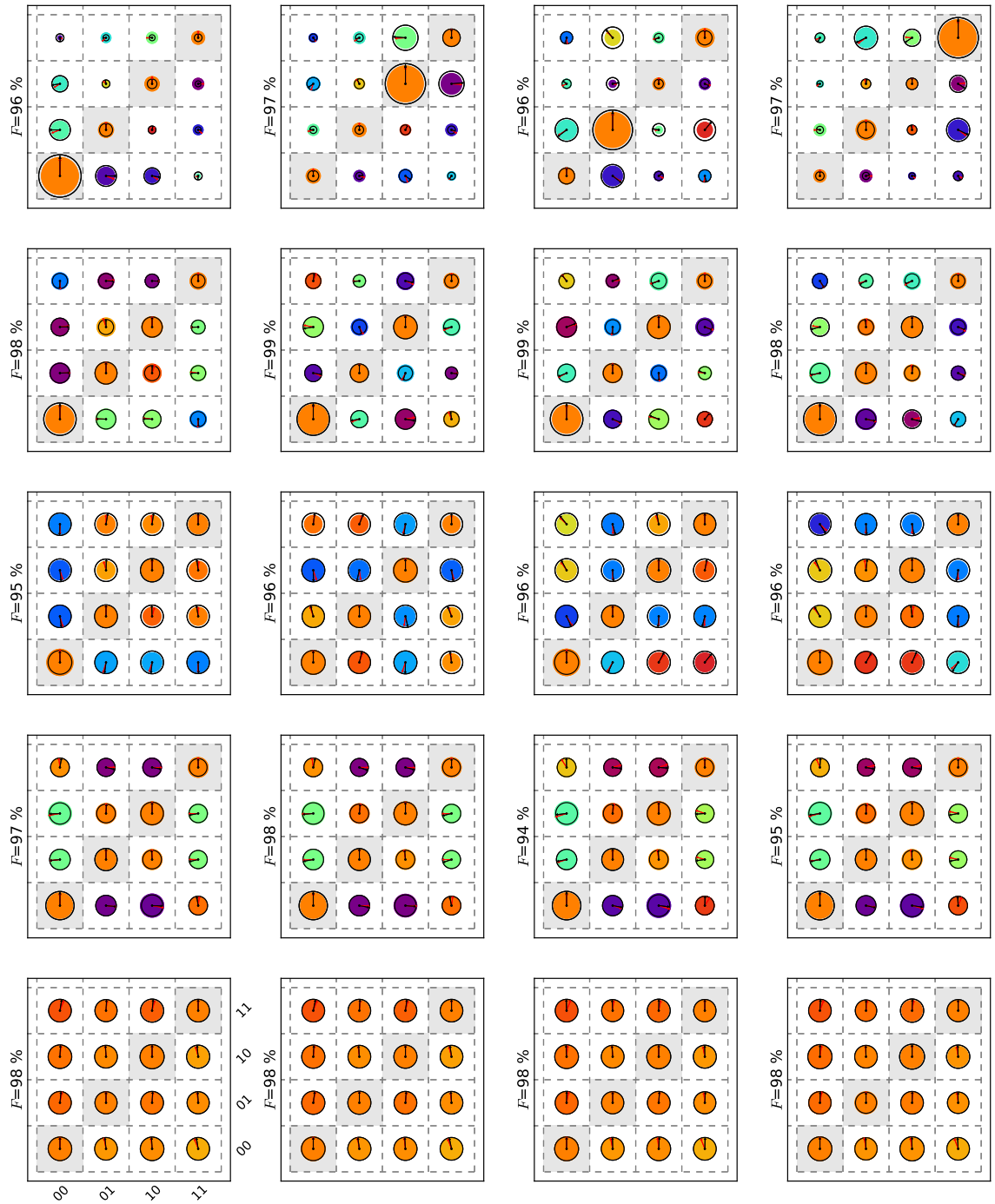


Figure 7.8: Quantum state tomographies at different steps of the Grover search algorithm and single-run outcome probabilities. The density matrices show the experimentally measured states in color and the theoretical states in black. For each state, the trace fidelity $F_{tr}(\rho_A, \rho_B) = \text{Tr}\{\rho_A \cdot \rho_B\}$ is shown above the density matrix.

measured quantum states before applying each of the operators as input. We take as the fidelity of each operator the average state fidelity of the measured output states as compared to the calculated ones, such that

$$F(D'_e) = F(D'\rho_{in}D'^\dagger, D'_e\rho_{in}D_e'^\dagger) \quad (7.18)$$

$$F(R'_e) = F(R'\rho_{in}R'^\dagger, R'_e\rho_{in}R_e'^\dagger) \quad (7.19)$$

where we also use the state fidelity according to eq. ???. By this method, we obtain the following fidelities for the two gate operations:

Operator / State	$ 00\rangle$	$ 01\rangle$	$ 10\rangle$	$ 11\rangle$	Average
D'	92.3	93.4	94.3	91.7	92.9
R'	94.5	93.6	88.5	87.7	91.1

Table 7.3: Measured fidelities of the quantum Oracle and diffusion operators used in the Grover search algorithm according to eqs. (7.18) and (7.19). All fidelities are given in percent.

7.5.2 Readout Errors

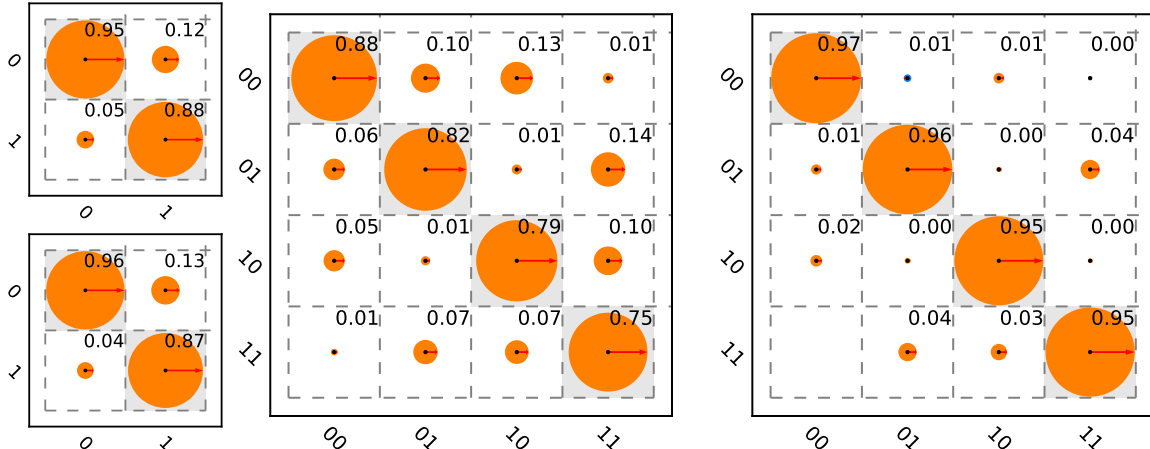


Figure 7.9: a.)The measured single-qubit readout matrices, showing the readout outcome probabilities as a function of the prepared state for both qubits. b.)The measured two-qubit radout matrix, showing again the detector outcome probabilities versus the prepared qubit states. c.) The crosstalk matrix, corresponding to the product of the two-qubit readout matrix and the Kronecker product of the single-qubit readout matrices. Note that the $|1\rangle \rightarrow |2\rangle$ shelving method is used for reading out the qubit state, which increases readout fidelity but also inter-qubit readout crosstalk.

Another source of errors arises due to the imperfection of our qubit readout. Mostly, qubit relaxation during the readout process reduces the visibility of individual qubit states

and introduces errors when reading out the qubit register in the final step of the algorithm. We can easily quantify those readout errors by using the readout matrix that was introduced in the last chapter. Fig. ?? shows this matrix for our experiment. We use the $|1\rangle \rightarrow |2\rangle$ shelving method described in the last chapter to increase the readout contrast, which reduces single-qubit readout but increases inter-qubit readout crosstalk. To quantify single-qubit and inter-qubit readout errors, we can split up the readout matrix R such that $R = R_v \cdot R_{ct}$, where R_v is the so-called *visibility matrix* that can be written as the Kronecker product $R_v = R_v^1 \otimes R_v^2$ of two single-qubit readout matrices of the form

$$R_v^{1,2} = \begin{pmatrix} p_{00}^{1,2} & 1 - p_{11}^{1,2} \\ 1 - p_{00}^{1,2} & p_{11}^{1,2} \end{pmatrix} \quad (7.20)$$

Here, $p_{00}^{1,2}$ ($p_{11}^{1,2}$) gives the probability to obtain the readout value 0 (1) when the qubit has been prepared in state $|0\rangle$ ($|1\rangle$).

Fig. 7.5e shows the single-run probabilities when running the Grover algorithm for the four different Oracle functions. In blue, the expected readout outcome probabilities, as calculated using the state tomography of the final states given in fig. 7.5d and the measured readout matrix of our system are shown along the measured readout outcome probabilities. The readout error model shows good quantitative agreement with the measured data, with deviations most probably due to parameter drifts occurred between the measurement of the quantum state tomography and the single-run experiment.

7.6 Conclusions

To summarize, we have shown that we can implement the Grover search algorithm with our quantum processor and achieve a single-run fidelity that is sufficient to demonstrate simple probabilistic quantum speed-up as compared to a classical, reversible search algorithm. The error model formulated in this chapter is able to account for most of the observed imperfections and can explain the data we observed. The coherence times of our qubits does not permit the realization of more complex algorithm with this system, nevertheless it provides a proof-of-principle of our approach to build a superconducting quantum computer with individual-qubit single shot readout.

In the following chapter, we will discuss the extension of this approach to a system of four qubits and explain different strategies for scaling up such system to an even larger number of qubits.

Chapter 8

Designing a Scalable Architecture for Quantum Bits

8.1 Definition & Requirements

8.2 Qubit Design

8.2.1 Qubit Parameters

8.2.2 Qubit-Qubit Coupling

8.3 Readout Design

8.3.1 Readout Parameters

8.3.2 Qubit-Readout Coupling

8.4 Single-Qubit Manipulation

8.4.1 Error Analysis

8.5 Multi-Qubit Manipulation

8.5.1 Error Analysis

8.6 Implementing a Universal Set of Quantum Gates

8.7 Realizing A Four-Qubit Architecture

8.8 Scaling Up

Chapter 9

Conclusions & Outlook

9.1 Future Directions in Superconducting QC

9.1.1 3D Circuit Quantum Electrodynamics

9.1.2 Hybrid Quantum Systems

9.1.3 Quantum Error Correction & Feedback

Appendix A

Modeling of Multi-Qubit Systems

A.1 Analytical Approach

A.1.1 Multi-Qubit Hamiltonian

A.1.2 Energies and Eigenstates

A.2 Master Equation Approach

$$\frac{d\rho}{dt} = -\frac{i}{\hbar}[H, \rho] + \sum_j [2L_j \rho L_j^\dagger - \{L_j^\dagger L_j, \rho\}] \quad (\text{A.1})$$

A.2.1 Direct Integration

A.2.2 Monte Carlo Simulation

A.2.3 Speeding Up Simulations

Appendix B

Data Acquisition & Management

B.1 Data Acquisition Infrastructure

B.2 Data Management Requirements

B.3 PyView

B.3.1 Overview

B.3.2 Instrument Management

B.3.3 Data Acquisition

B.3.4 Data Management

B.3.5 Data Analysis

Appendix C

Design & Fabrication

C.1 Mask Design

C.2 Optical Lithography

C.3 Electron Beam Lithography

Bibliography

- Blais, A., Huang, R., Wallraff, A., Girvin, S. M., and Schoelkopf, R. J. (2004). Cavity quantum electrodynamics for superconducting electrical circuits: An architecture for quantum computation. *Physical Review A*, 69(6):062320.
- Chiorescu, I., Nakamura, Y., Harmans, C. J. P. M., and Mooij, J. E. (2003). Coherent quantum dynamics of a superconducting flux qubit. *Science*, 299(5614):1869–1871.
- Clauser, J. F., Horne, M. A., Shimony, A., and Holt, R. A. (1969). Proposed experiment to test local Hidden-Variable theories. *Physical Review Letters*, 23(15):880–884.
- Collin, E., Ithier, G., Aassime, A., Joyez, P., Vion, D., and Esteve, D. (2004). NMR-like control of a quantum bit superconducting circuit. *Physical Review Letters*, 93(15):157005.
- Cottet, A. (2002). *Implementation of a quantum bit in a superconducting circuit*. PhD thesis, Université Paris VI, Paris.
- DiCarlo, L., Chow, J. M., Gambetta, J. M., Bishop, L. S., Johnson, B. R., Schuster, D. I., Majer, J., Blais, A., Frunzio, L., Girvin, S. M., and Schoelkopf, R. J. (2009). Demonstration of two-qubit algorithms with a superconducting quantum processor. *Nature*, 460(7252):240–244.
- DiCarlo, L., Reed, M. D., Sun, L., Johnson, B. R., Chow, J. M., Gambetta, J. M., Frunzio, L., Girvin, S. M., Devoret, M. H., and Schoelkopf, R. J. (2010). Preparation and measurement of three-qubit entanglement in a superconducting circuit. *Nature*, 467(7315):574–578.
- DiVincenzo, D. P. (2000). The physical implementation of quantum computation. *Fortschritte der Physik*, 48(9-11):771–783.
- Grover, L. K. (1997). Quantum mechanics helps in searching for a needle in a haystack. *Physical Review Letters*, 79(2):325–328.
- Grover, L. K. (2001). From schrödinger's equation to the quantum search algorithm. *American Journal of Physics*, 69(7):769–777.

- Haroche, S. and Raimond, J. (2006). *Exploring the Quantum: Atoms, Cavities and Photons*. Oxford University Press.
- Koch, J., Yu, T. M., Gambetta, J., Houck, A. A., Schuster, D. I., Majer, J., Blais, A., Devoret, M. H., Girvin, S. M., and Schoelkopf, R. J. (2007). Charge-insensitive qubit design derived from the cooper pair box. *Physical Review A*, 76(4):042319.
- Lanyon, B. P., Hempel, C., Nigg, D., Müller, M., Gerritsma, R., Zähringer, F., Schindler, P., Barreiro, J. T., Rambach, M., Kirchmair, G., Hennrich, M., Zoller, P., Blatt, R., and Roos, C. F. (2011). Universal digital quantum simulation with trapped ions. *Science*, 334(6052):57–61.
- Lloyd, S. (1996). Universal quantum simulators. *Science*, 273(5278):1073–1078.
- Majer, J., Chow, J. M., Gambetta, J. M., Koch, J., Johnson, B. R., Schreier, J. A., Frunzio, L., Schuster, D. I., Houck, A. A., Wallraff, A., Blais, A., Devoret, M. H., Girvin, S. M., and Schoelkopf, R. J. (2007). Coupling superconducting qubits via a cavity bus. *Nature*, 449(7161):443–447.
- Mallet, F., Ong, F. R., Palacios-Laloy, A., Nguyen, F., Bertet, P., Vion, D., and Esteve, D. (2009). Single-shot qubit readout in circuit quantum electrodynamics. *Nat Phys*, 5(11):791–795.
- Martinis, J. M., Devoret, M. H., and Clarke, J. (1985). Energy-Level quantization in the Zero-Voltage state of a Current-Biased josephson junction. *Physical Review Letters*, 55(15):1543–1546.
- Martinis, J. M., Nam, S., Aumentado, J., and Urbina, C. (2002). Rabi oscillations in a large Josephson-Junction qubit. *Physical Review Letters*, 89(11):117901.
- Michael A. Nielsen and Isaac L. Chuang (2000). *Quantum Computation and Quantum Information*. Cambridge University Press.
- Mooij, J. E., Orlando, T. P., Levitov, L., Tian, L., van der Wal, C. H., and Lloyd, S. (1999). Josephson Persistent-Current qubit. *Science*, 285(5430):1036 –1039.
- Nakamura, Y., Pashkin, Y. A., and Tsai, J. S. (1999). Coherent control of macroscopic quantum states in a single-Cooper-pair box. *Nature*, 398(6730):786–788.
- Paik, H., Schuster, D. I., Bishop, L. S., Kirchmair, G., Catelani, G., Sears, A. P., Johnson, B. R., Reagor, M. J., Frunzio, L., Glazman, L. I., Girvin, S. M., Devoret, M. H., and Schoelkopf, R. J. (2011). Observation of high coherence in josephson junction qubits measured in a Three-Dimensional circuit QED architecture. *Physical Review Letters*, 107(24):240501.

- Palacios-Laloy, A. (2010). *Superconducting qubit in a resonator: Test of the Leggett-Garg inequality and single-shot readout*. PhD thesis, Université Paris VI, Paris.
- Siddiqi, I., Vijay, R., Metcalfe, M., Boaknin, E., Frunzio, L., Schoelkopf, R. J., and Devoret, M. H. (2006). Dispersive measurements of superconducting qubit coherence with a fast latching readout. *Physical Review B*, 73(5):054510.
- Siddiqi, I., Vijay, R., Pierre, F., Wilson, C. M., Metcalfe, M., Rigetti, C., Frunzio, L., and Devoret, M. H. (2004). RF-Driven josephson bifurcation amplifier for quantum measurement. *Physical Review Letters*, 93(20):207002.
- Vijay, R., Devoret, M. H., and Siddiqi, I. (2009). Invited review article: The josephson bifurcation amplifier. *Review of Scientific Instruments*, 80(11):111101–111101–17.
- Vijay, R., Slichter, D. H., and Siddiqi, I. (2011). Observation of quantum jumps in a superconducting artificial atom. *Physical Review Letters*, 106(11):110502.
- Vion, D., Aassime, A., Cottet, A., Joyez, P., Pothier, H., Urbina, C., Esteve, D., and Devoret, M. H. (2002). Manipulating the quantum state of an electrical circuit. *Science*, 296(5569):886 –889.
- Wallraff, A., Schuster, D. I., Blais, A., Frunzio, L., Huang, R.-S., Majer, J., Kumar, S., Girvin, S. M., and Schoelkopf, R. J. (2004). Strong coupling of a single photon to a superconducting qubit using circuit quantum electrodynamics. *Nature*, 431(7005):162–167.